4-17-2018 10:00 AM

Compact Sensing Platforms Based on Localized Surface Plasmon Resonance

Zhutian Ding, *The University of Western Ontario*

Supervisor: Mittler, Silvia, *The University of Western Ontario*
A thesis submitted in partial fulfillment of the requirements for the Master of Science degree in Chemistry

Recommended Citation

Ding, Zhutian, "Compact Sensing Platforms Based on Localized Surface Plasmon Resonance" (2018). *Electronic Thesis and Dissertation Repository*. 5295.
https://ir.lib.uwo.ca/etd/5295

Compact Sensing Platforms Based on Localized Surface Plasmon Resonance

Abstract

The development of plasmonic sensors mainly focuses on the improvement of their sensitivities that are approaching the theoretical limit. This work aims to propose, fabricate and characterize compact sensing platforms that are highly adaptable and easy to be miniaturized, without compromising their sensitivities. A plasmonic sensing system that allows the excitation of localized surface plasmon resonance (LSPR) by individual waveguide modes is presented conceptually and experimentally. Another compact sensing platform is proposed based on the ensemble hypothesis developed in this thesis.

Keywords

Localized surface plasmon resonance, gold nanoparticles, plasmonic nanoparticles, biosensing, waveguide, organometallic chemical vapor deposition, self-assembled monolayer.

Co-Authorship Statement

Chapter 3 contains materials from Ding, Z., Stubbs, J., McRae, D., Blacquiere, J., Lagugné-Labarthet, F., Mittler, S., *A Mass-Producible and Versatile Sensing System: Localized Surface Plasmon Resonance Excited by Individual Waveguide Modes.* ACS Sensors, 2018. **3**(2): p. 334-341. James Stubbs performed the synthesis of methyl trimethylphosphine gold. Danielle McRae performed AFM measurement on the size of gold nanoparticles. Zhutian Ding performed the rest.

Chapter 4 contains materials from an accepted manuscript (in press) to the Journal of Physical Chemistry C. James Stubbs performed the synthesis of methyl trimethylphosphine gold. Zhutian Ding performed the rest.

Acknowledgments

This work would not have been possible without the guidance of my supervisor Dr. Silvia Mittler. Her patience and mentorship throughout my Master's career served as a cornerstone to the development of my research abilities. Thus, I gratefully acknowledge and thank her for her involvement in this process.

I would like to thank Dr. Erden Ertorer and Sivayini Kandeepan for their help on the know-how transfer of OMCVD techniques; Dr. Bernd Grohe and Tony Tran, our group members, for maintaining a collegial environment for me to work in.

I would like to thank Dr. Todd Simpson and Tim Goldhawk for helping me navigate through Western Nanofabrication Facility and for taking SEM images; Brian Dalrymple and Frank Van Sas from the Physics Machine Shop for crafting the pieces crucial to my optical experiments.

Table of Contents

List of Tables

List of Figures

List of Appendices

List of Symbols and Abbreviations

a.u.	arbitrary absorption unit
c	speed of light in vacuum
d	thickness of waveguides
$\vec{E}$	electric field
e	charge of an electron
$\hbar$	reduced Planck constant $h/(2\pi)$
$\vec{k}$	wave vector of incident electromagnetic wave in the medium specified $\lvert\vec{k}\rvert = 2\pi n(\omega)/\lambda_0 = \sqrt{\varepsilon_m}(\omega/c)$. $n(\omega)$ is the refractive index of the medium specified. ω is the angular frequency of electromagnetic waves. ε_m is the dielectric function of the medium specified. λ_0 is the wavelength in vacuum. $\lvert\vec{k}\rvert$ is denoted as k in this thesis.
$\mathbf{k}$	reciprocal lattice vector
n	refractive index
$\vec{r}$	position vector
R	cluster radius
V	volume of a spherical particle $V = (4\pi/3)R^3$
α	polarizability
Γ	FWHM of LSPR curves
ε, ε_m	complex dielectric function $\varepsilon = \varepsilon_1 + i\varepsilon_2$, of cluster or medium
λ	wavelength of electromagnetic wave in the medium specified

ν	frequency
σ	cross section
χ	susceptibility ($\varepsilon=1+\chi$)
ψ	wave function
ω_p	plasma frequency
ω	angular frequency of incident electro-magnetic wave

AFM	Atomic Force Microscopy
AuNPs	Gold Nanoparticles
DDA	Discrete Dipole Approximation
ELW	Ensemble Linewidth
FDTD	Finite Difference Time Domain
FOM	Figure of Merit
FWHM	Full Width at Half Maximum
IONA	Index of Nanoparticle Absorption
IOWA	Index of Waveguide Absorption
LSPR	Localized Surface Plasmon Resonance
OMCVD	Organometallic Chemical Vapour Deposition
RIU	Refractive Index Unit
SAM	Self-Assembled Monolayer

SEM	Scanning Electron Microscopy
TE	Transverse Electric
TIR	Total Internal Reflection
TM	Transverse Magnetic

1 Introduction and Overview of the Thesis

Localized surface plasmon resonance (LSPR) in noble metal nanoparticles occurs when the frequency of the incident photons matches the oscillation frequency of their conduction electrons. LSPR of noble metal nanostructures leads to intense spectral extinctions in the UV-visible region and creates strong near-field enhancements in forms of evanescent fields [1]. The typical extinction coefficient of plasmonic nanoparticles is on the order of 10^{11} $M^{-1}cm^{-1}$, with efficiency equivalent to that of 10^6 fluorophores [2]. Due to their extraordinary optical properties, plasmonic nanoparticles are widely used in immunoassays [3-5], biochemical sensors [2, 6-10], surface-enhanced spectroscopies [11-16], and many more [17].

This thesis focuses on the sensing applications of gold nanoparticles (AuNPs). The LSPR wavelength of AuNPs is very sensitive to their local refractive index, rendering them valuable transducers that convert small optical changes in the local environment into spectral shifts. The majority of the plasmonic sensors reported monitor the shift of plasmon peak wavelength of either colloidal [18-19] or surface immobilized nanoparticles [20-25]. Peak intensity [26], curvature [27] and inflection point [28] have also been reported to be quantitative indicators of the local refractive index.

In contrast to the vast majority of biological sensors, LSPR based sensors are label-free because they detect the change of local refractive index due to the presence of target molecules directly. This feature allows detailed measurements being performed on biomolecules in their natural states. Moreover, thanks to their small sizes and their highly localized field enhancements due to LSPR, plasmonic nano-sensors require only a minuscule amount of analytes and are resistant to bulk noises. The most widely used immunoassay, ELISA, is a typical end-point assay because its signal is generated after the target antigen captures a second antigen. In comparison, LSPR based sensors not only allow real-time measurements, but also only require the capture of a single antigen [1]. They indeed have great potentials to be the next generation biosensors.

Significant research has been dedicated to exploring the biosensing abilities of plasmonic nanoparticles. The classic biotin-streptavidin system is often used in developing biosensors due to the strong and specific bond formed and the availability of related bioconjugate techniques. Many reports have been published on the measurements of such system using LSPR assays in various biological media such as serum, diluted blood and saline [23, 29-33]. Other biological interactions, such as antigen-antibody [34-36], DNA hybridization [37], protein-carbohydrate [38], cytochrome-substrate[39], and enzyme-inhibitor [40].

LSPR sensors need to be engineered before they can compete with common assays such as ELISA. Multiplexing technology enables multiple parallel measurements that can lead to rapid and systematic diagnoses because all samples are measured at the same time against the same reference [41]. Endo et al. [42] fabricated a plasmonic chip with arrays of fine structures about 1 nm apart and conducted measurements on 300 antibody-antigen reactions by depositing nanolitres of antibody solutions on functionalized gold nanospheres. Yonzon et al. [43-44] utilized a different strategy in that two types of silver nanotriangles were fabricated. As a result, the spectral shifts could be resolved without any special instrumentation because the two types peak in different spectral regions.

LSPR sensors also need to be integrated with microfluidics for practical applications so that only small sample volumes are necessary. High speed and high throughput are the two main advantages of microfluidic systems. Huang et al. [45] developed an LSPR-microfluidic chip with automated sampling system that only required a sample volume of 2.5 µL. Further improvements are needed to scale up the system and to read out the optical extinction from a large number of channels.

The objective of this thesis is to propose, design, and fabricate compact sensing platforms that can be easily adapted by others working with different types of plasmonic nanoparticles. Their compact nature ensures that they can be easily engineered into cost-effective and portable point-of-care devices.

The second chapter covers the fundamental physics needed to fully understand this thesis. The third chapter describes the development, fabrication, characterization, and optimization strategies of a sensing platform based on the degree of coupling between AuNPs and a planar waveguide. The fourth chapter proposes an ensemble hypothesis along with spectroscopic evidence to explain the narrowing behaviour of ensemble LSPR peaks upon the functionalization of AuNPs. A compact sensing platform is proposed based on the ensemble hypothesis. The fifth chapter summarizes the conclusions and future work.

1.1 References

1. Mayer, K. M.; Hafner, J. H., Localized Surface Plasmon Resonance Sensors. *Chemical Reviews* **2011,** *111* (6), 3828-3857.

2. McFarland, A. D.; Van Duyne, R. P., Single Silver Nanoparticles as Real-Time Optical Sensors with Zeptomole Sensitivity. *Nano Letters* **2003,** *3* (8), 1057-1062.

3. Schultz, S.; Smith, D. R.; Mock, J. J.; Schultz, D. A., Single-target molecule detection with nonbleaching multicolor optical immunolabels. *Proceedings of the National Academy of Sciences* **2000,** *97* (3), 996.

4. Nam, J.-M.; Thaxton, C. S.; Mirkin, C. A., Nanoparticle-Based Bio-Bar Codes for the Ultrasensitive Detection of Proteins. *Science* **2003,** *301* (5641), 1884.

5. Yguerabide, J.; Yguerabide, E. E., Light-Scattering Submicroscopic Particles as Highly Fluorescent Analogs and Their Use as Tracer Labels in Clinical and Biological Applications: I. Theory. *Analytical Biochemistry* **1998,** *262* (2), 137-156.

6. Yonzon, C. R.; Stuart, D. A.; Zhang, X.; McFarland, A. D.; Haynes, C. L.; Van Duyne, R. P., Towards advanced chemical and biological nanosensors—An overview. *Talanta* **2005,** *67* (3), 438-448.

7. Haes, A. J.; Chang, L.; Klein, W. L.; Van Duyne, R. P., Detection of a Biomarker for Alzheimer's Disease from Synthetic and Clinical Samples Using a Nanoscale Optical Biosensor. *Journal of the American Chemical Society* **2005,** *127* (7), 2264-2271.

8. Elghanian, R.; Storhoff, J. J.; Mucic, R. C.; Letsinger, R. L.; Mirkin, C. A., Selective Colorimetric Detection of Polynucleotides Based on the Distance-Dependent Optical Properties of Gold Nanoparticles. *Science* **1997,** *277* (5329), 1078.

9. Raschke, G.; Kowarik, S.; Franzl, T.; Sönnichsen, C.; Klar, T. A.; Feldmann, J.; Nichtl, A.; Kürzinger, K., Biomolecular Recognition Based on Single Gold Nanoparticle Light Scattering. *Nano Letters* **2003,** *3* (7), 935-938.

10. Dahlin, A. B.; Tegenfeldt, J. O.; Höök, F., Improving the Instrumental Resolution of Sensors Based on Localized Surface Plasmon Resonance. *Analytical Chemistry* **2006,** *78* (13), 4416-4423.

11. Dieringer, J. A.; McFarland, A. D.; Shah, N. C.; Stuart, D. A.; Whitney, A. V.; Yonzon, C. R.; Young, M. A.; Zhang, X.; Van Duyne, R. P., Introductory Lecture Surface enhanced Raman spectroscopy: new materials, concepts, characterization tools, and applications. *Faraday Discussions* **2006,** *132* (0), 9-26.

12. Haller, K. L.; Bumm, L. A.; Altkorn, R. I.; Zeman, E. J.; Schatz, G. C.; Van Duyne, R. P., Spatially resolved surface enhanced second harmonic generation: Theoretical and experimental evidence for electromagnetic enhancement in the near infrared on a laser microfabricated Pt surface. *The Journal of Chemical Physics* **1989,** *90* (2), 1237-1252.

13. Yang, W. H.; Hulteen, J.; Schatz, G. C.; Van Duyne, R. P., A surface-enhanced hyper-Raman and surface-enhanced Raman scattering study of frans-1,2-bis(4-pyridyl)ethylene adsorbed onto silver film over nanosphere electrodes. Vibrational assignments: Experiment and theory. *Journal of Chemical Physics* **1996,** *104* (11), 4313-4323.

14. Jensen, T. R.; Duyne, R. P. V.; Johnson, S. A.; Maroni, V. A., Surface-Enhanced Infrared Spectroscopy: A Comparison of Metal Island Films with Discrete and Nondiscrete Surface Plasmons. *Applied Spectroscopy* **2000,** *54* (3), 371-377.

15. Moskovits, M., Surface-enhanced spectroscopy. *Reviews of Modern Physics* **1985,** *57* (3), 783-826.

16. Chen, Y.; Munechika, K.; Ginger, D. S., Dependence of Fluorescence Intensity on the Spectral Overlap between Fluorophores and Plasmon Resonant Single Silver Nanoparticles. *Nano Letters* **2007,** *7* (3), 690-696.

17. Homola, J., Surface Plasmon Resonance Sensors for Detection of Chemical and Biological Species. *Chemical Reviews* **2008,** *108* (2), 462-493.

18. Englebienne, P., Use of colloidal gold surface plasmon resonance peak shift to infer affinity constants from the interactions between protein antigens and antibodies specific for single or multiple epitopes. *Analyst* **1998,** *123* (7), 1599-1603.

19. Li, X.; Jiang, L.; Zhan, Q.; Qian, J.; He, S., Localized surface plasmon resonance (LSPR) of polyelectrolyte-functionalized gold-nanoparticles for bio-sensing. *Colloids and Surfaces A: Physicochemical and Engineering Aspects* **2009,** *332* (2), 172-179.

20. Grabar, K. C.; Freeman, R. G.; Hommer, M. B.; Natan, M. J., Preparation and Characterization of Au Colloid Monolayers. *Analytical Chemistry* **1995,** *67* (4), 735-743.

21. Okamoto, T.; Yamaguchi, I.; Kobayashi, T., Local plasmon sensor with gold colloid monolayers deposited upon glass substrates. *Optics Letters* **2000,** *25* (6), 372-374.

22. Haes, A. J.; Duyne, R. P. V., Preliminary studies and potential applications of localized surface plasmon resonance spectroscopy in medical diagnostics. *Expert Review of Molecular Diagnostics* **2004,** *4* (4), 527-537.

23. Haes, A. J.; Van Duyne, R. P., A Nanoscale Optical Biosensor: Sensitivity and Selectivity of an Approach Based on the Localized Surface Plasmon Resonance Spectroscopy of Triangular Silver Nanoparticles. *Journal of the American Chemical Society* **2002,** *124* (35), 10596-10604.

24. Nath, N.; Chilkoti, A., Label-Free Biosensing by Surface Plasmon Resonance of Nanoparticles on Glass: Optimization of Nanoparticle Size. *Analytical Chemistry* **2004,** *76* (18), 5370-5378.

25. Fan, M.; Thompson, M.; Andrade, M. L.; Brolo, A. G., Silver Nanoparticles on a Plastic Platform for Localized Surface Plasmon Resonance Biosensing. *Analytical Chemistry* **2010,** *82* (15), 6350-6352.

26. Lin, H.-Y.; Chen, C.-T.; Chen, Y.-C., Detection of Phosphopeptides by Localized Surface Plasma Resonance of Titania-Coated Gold Nanoparticles Immobilized on Glass Substrates. *Analytical Chemistry* **2006,** *78* (19), 6873-6878.

27. Chen, P.; Liedberg, B., Curvature of the Localized Surface Plasmon Resonance Peak. *Analytical Chemistry* **2014,** *86* (15), 7399-7405.

28. Chen, P.; Tran, N. T.; Wen, X.; Xiong, Q.; Liedberg, B., Inflection Point of the Localized Surface Plasmon Resonance Peak: A General Method to Improve the Sensitivity. *ACS Sensors* **2017,** *2* (2), 235-242.

29. Marinakos, S. M.; Chen, S.; Chilkoti, A., Plasmonic Detection of a Model Analyte in Serum by a Gold Nanorod Sensor. *Analytical Chemistry* **2007,** *79* (14), 5278-5283.

30. Chen, C.-D.; Cheng, S.-F.; Chau, L.-K.; Wang, C. R. C., Sensing capability of the localized surface plasmon resonance of gold nanorods. *Biosensors and Bioelectronics* **2007,** *22* (6), 926-932.

31. Arai, T.; Kumar, P. K. R.; Rockstuhl, C.; Awazu, K.; Tominaga, J., An optical biosensor based on localized surface plasmon resonance of silver nanostructured films. *Journal of Optics A: Pure and Applied Optics* **2007,** *9* (7), 699.

32. Wang, Y.; Qian, W.; Tan, Y.; Ding, S., A label-free biosensor based on gold nanoshell monolayers for monitoring biomolecular interactions in diluted whole blood. *Biosensors and Bioelectronics* **2008,** *23* (7), 1166-1170.

33. Kazuma, E.; Tatsuma, T., Localized surface plasmon resonance sensors based on wavelength-tunable spectral dips. *Nanoscale* **2014,** *6* (4), 2397-2405.

34. Anker, J. N.; Hall, W. P.; Lambert, M. P.; Velasco, P. T.; Mrksich, M.; Klein, W. L.; Van Duyne, R. P., Detection and Identification of Bioanalytes with High Resolution LSPR Spectroscopy and MALDI Mass Spectrometry. *The Journal of Physical Chemistry C* **2009,** *113* (15), 5891-5894.

35. Kreuzer, M. P.; Quidant, R.; Salvador, J. P.; Marco, M. P.; Badenes, G., Colloidal-based localized surface plasmon resonance (LSPR) biosensor for the quantitative determination of stanozolol. *Analytical and Bioanalytical Chemistry* **2008,** *391* (5), 1813-1820.

36. Byun, J.-Y.; Shin, Y.-B.; Li, T.; Park, J.-H.; Kim, D.-M.; Choi, D.-H.; Kim, M.-G., The use of an engineered single chain variable fragment in a localized surface plasmon resonance method for analysis of the C-reactive protein. *Chemical Communications* **2013,** *49* (82), 9497-9499.

37. Yoo, S. Y.; Kim, D.-K.; Park, T. J.; Kim, E. K.; Tamiya, E.; Lee, S. Y., Detection of the Most Common Corneal Dystrophies Caused by BIGH3 Gene Point Mutations Using a Multispot Gold-Capped Nanoparticle Array Chip. *Analytical Chemistry* **2010,** *82* (4), 1349-1357.

38. Morokoshi, S.; Ohhori, K.; Mizukami, K.; Kitano, H., Sensing Capabilities of Colloidal Gold Modified with a Self-Assembled Monolayer of a Glucose-Carrying Polymer Chain on a Glass Substrate. *Langmuir* **2004,** *20* (20), 8897-8902.

39. Zhao, J.; Das, A.; Schatz, G. C.; Sligar, S. G.; Van Duyne, R. P., Resonance Localized Surface Plasmon Spectroscopy: Sensing Substrate and Inhibitor Binding to Cytochrome P450. *The Journal of Physical Chemistry C* **2008,** *112* (34), 13084-13088.

40. Lin, T.-J.; Huang, K.-T.; Liu, C.-Y., Determination of organophosphorous pesticides by a novel biosensor based on localized surface plasmon resonance. *Biosensors and Bioelectronics* **2006,** *22* (4), 513-518.

41. Unser, S.; Bruzas, I.; He, J.; Sagle, L., Localized Surface Plasmon Resonance Biosensing: Current Challenges and Approaches. *Sensors (Basel, Switzerland)* **2015,** *15* (7), 15684-15716.

42. Endo, T.; Kerman, K.; Nagatani, N.; Hiepa, H. M.; Kim, D.-K.; Yonezawa, Y.; Nakano, K.; Tamiya, E., Multiple Label-Free Detection of Antigen−Antibody Reaction Using Localized Surface Plasmon Resonance-Based Core−Shell Structured Nanoparticle Layer Nanochip. *Analytical Chemistry* **2006,** *78* (18), 6465-6475.

43. Yonzon, C. R.; Jeoung, E.; Zou, S.; Schatz, G. C.; Mrksich, M.; Van Duyne, R. P., A Comparative Analysis of Localized and Propagating Surface Plasmon Resonance Sensors: The Binding of Concanavalin A to a Monosaccharide Functionalized Self-Assembled Monolayer. *Journal of the American Chemical Society* **2004,** *126* (39), 12669-12676.

44. Zhao, J.; Zhang, X.; Yonzon, C. R.; Haes, A. J.; Duyne, R. P. V., Localized surface plasmon resonance biosensors. *Nanomedicine* **2006,** *1* (2), 219-228.

45. Huang, C.; Bonroy, K.; Reekman, G.; Verstreken, K.; Lagae, L.; Borghs, G., An on-chip localized surface plasmon resonance-based biosensor for label-free monitoring of antigen–antibody reaction. *Microelectronic Engineering* **2009,** *86* (12), 2437-2441.

2 Fundamentals

2.1 Optical Properties of Noble Nanoparticles

2.1.1 A Semi-Classical Extension of the Drude Model

Unlike the alkali metals, interband transitions from lower-lying bands into the conduction band or from the conduction band into higher unoccupied levels contribute substantially to the dielectric function of noble metals. In this section, the linewidth and the frequency of LSPR spectra for noble metals are discussed by considering the contribution of interband transitions to the dielectric function, $\varepsilon(\omega)$, of free-electron metals that follow the Drude model in the quasi-static regime [46].

Consider spherical metallic particles embedded in an isotropic homogeneous non-absorbing matrix with dielectric constant ε_m. It is assumed that the radius of the particles is small enough ($R \ll \lambda$) such that the external electric field can be treated as time dependent but spatially homogeneous. In this quasi-static approximation, the particles are treated as single dipoles reacting to the external field and retardation effects are ignored. Due to their small size, the absorption cross section, $\sigma_{abs}(\omega)$, has a dominant contribution to the extinction of light [47]:

$$\sigma_{abs}(\omega) = k \cdot \mathrm{Im}(\alpha(\omega)) \tag{1}$$

where $\alpha(\omega)$ is the polarizability of the particle, and $k = \sqrt{\varepsilon_m}(\omega/c)$ is the magnitude of the wave vector of the incident light in a certain medium. The interband susceptibility can be expressed as $\chi^{ib}(\omega) = \chi_1^{ib}(\omega) + i\chi_2^{ib}(\omega)$. $\chi_1^{ib}(\omega)$ is delocalized on the frequency scale whereas $\chi_1^{ib}(\omega)$ is only significant beyond the interband transition threshold (ω_i). Thus, the corrected dielectric function is:

$$\varepsilon(\omega) = 1 - \frac{\omega_p{}^2}{\omega^2 + i\gamma\omega} + \chi^{ib}(\omega) \tag{2}$$

where ω_p is the plasma frequency of the conduction electrons and γ is the rate of electron collisions. The polarizability of spherical particles with only $\chi_1^{ib}(\omega)$ taken into account, leads to [47]:

$$\alpha(\omega) = 4\pi R^3 \frac{(1+\chi_1{}^{ib}-\varepsilon_m)}{(1+\chi_1{}^{ib}+2\varepsilon_m)} + \frac{12\pi R^3 \varepsilon_m}{(1+\chi_1{}^{ib}+2\varepsilon_m)} \frac{\Omega^2}{(\Omega^2-\omega^2-i\gamma\omega)} \tag{3}$$

with the frequency:

$$\Omega = \frac{\omega_p}{\sqrt{1+\chi_1{}^{ib}+2\varepsilon_m}} \tag{4}$$

The absorption cross section is obtained by substituting equation 3 into 1:

$$\sigma_{abs}(\omega) = \frac{9V}{c} \frac{\varepsilon_m{}^{3/2}}{(1+\chi_1{}^{ib}+2\varepsilon_m)} \frac{\Omega^2\gamma\omega^2}{(\Omega^2-\omega^2)^2+(\gamma\omega)^2} \tag{5}$$

where V is the particle volume. LSPR corresponds to the maximum absorption cross section that occurs when $\omega = \Omega$. Assuming ε_m and γ are independent of ω, expressions for frequencies ω_1 and ω_2 are obtained that define the homogeneous linewidth of the LSPR spectrum, Γ. Subtracting the two, delivers the value of linewidth ($\Gamma = \gamma$). Thus, when the incident frequency is below the interband threshold of metal particles ($\chi_2{}^{ib} \rightarrow 0$), Γ has the same value as in free-electron metals [46-47].

A basic expression for χ^{ib} using the electric-dipole approximation for the electron-photon-interaction-Hamiltonian of direct transitions was developed by Bassani and Parravicini [48]. By treating the Hamiltonian as a first-order time-dependent perturbation term on the electronic states of the noble metals, the phenomenological interband susceptibility can be derived from the transition probability rate:

$$\chi^{ib} = \frac{8\hbar^3\pi e^2}{m_{eff}{}^2} \sum_{i,f} \int_{BZ} \frac{2d\mathbf{k}}{(2\pi)^3} |\mathbf{e}M_{if}(\mathbf{k})|^2 \left\{ \frac{1}{[E_f(\mathbf{k})-E_i(\mathbf{k})]\left[\left(E_f(\mathbf{k})-E_i(\mathbf{k})\right)^2-\hbar^2\omega^2\right]} + i\frac{\pi}{2\hbar^3\omega^2}\delta[E_f(\mathbf{k}) - E_i(\mathbf{k}) - \hbar\omega] \right\} \tag{6}$$

where m_{eff} is the effective electron mass that accounts for the coupling between free electrons and the ion core. **e** is a unit vector in the polarization direction of the incident electric field. The integral with respect to the reciprocal lattice vector, **k**, is over the first Brillouin zone (BZ). M_{if} is the matrix element of the dipole operator $M_{if} = \langle\psi_i|\mathbf{e}\mathbf{r}|\psi_f\rangle$ with ψ_i and ψ_f denoting the initial and final state. Assuming the matrix elements are constant throughout the Brillouin zone, one can compute χ_1^{ib} and χ_2^{ib}, respectively, from the real and the complex part of equation (6).

The Drude model treats electron oscillation as a collective event followed by a relaxation process dominated by single-electron collisions. This separate treatment leads to an inherent inconsistency because the real and imaginary parts of a dielectric function are connected by Kramers-Kronig relationship.

2.1.2 Mie Theory and Numerical Methods

The above discussion of quasi-static approximation fails for particles larger than 20 nm in diameter. Mie theory, as a more general model, is the exact solution of Maxwell's equations that describes light extinction behaviour of spherical or infinite cylindrical particles of arbitrary size and material [49-50]. The solutions are obtained by solving Maxwell's equations in spherical polar or cylindrical coordinates with boundary conditions defined by electron densities for the fields at the surface of the particles. Extinction, scattering and absorption cross sections are calculated by series expansions of the involved fields into partial waves of different spherical symmetries:

$$\sigma_{\mathrm{ext}} = \frac{2\pi}{k^2}\sum_{L=1}^{\infty}(2L+1)\mathrm{Re}(a_L+b_L) \tag{7}$$

$$\sigma_{\mathrm{sca}} = \frac{2\pi}{k^2}\sum_{L=1}^{\infty}(2L+1)(|a_L|^2+|b_L|^2) \tag{8}$$

with

$$a_L = \frac{m\psi_L(mx)\psi'_L(x)-\psi'_L(mx)\psi_L(x)}{m\psi_L(mx)\eta'_L(x)-\psi'_L(mx)\eta_L(x)} \tag{9}$$

$$b_L = \frac{\psi_L(mx)\psi'_L(x)-m\psi'_L(mx)\psi_L(x)}{\psi_L(mx)\eta'_L(x)-m\psi'_L(mx)\eta_L(x)} \tag{10}$$

with $m = n/n_m$, and n the complex refractive index of the particle and n_m the real refractive index of the medium. $x = kR$ is the size parameter. $\psi_L(z)$ and $\eta_L(z)$ are Riccati-Bessel cylindrical functions [51]. The prime denotes differentiation with respect to the variable in parentheses. The summation index L indicates the order of spherical multipole excitations in the particles: L = 1 corresponds to dipole modes (both electric and magnetic), L = 2 to quadrupole and so on. Extensions of the Mie theory that account for non-spherical geometries, core-shell structures, absorbing medium, and many more situations are summarized by Hergert and Wriedt [52].

Several numerical methods have been developed to perform quantitative evaluation of the optical response of nanoparticles when the situation cannot be solved analytically using electrodynamics or when the extended Mie methods get very tedious. An overview of the most commonly used method, discrete dipole approximation (DDA), is given [53-56]. For other significant numerical methods such as finite element method [57], finite difference time domain (FDTD) [58], and dyadic Green's function method [59], please consult the respective references.

DDA is a frequency domain approach that represents nanoparticles of arbitrary geometry as a cubic array of N polarizable elements. The polarizabilities (α_i, i = 1, 2, …, N) of individual dipoles are chosen so that the bulk material behaves the same as the continuum solution to Maxwell's equations. The dipole $\vec{P}_i$ induced by the local field $\vec{E}_{loc}$ at position $\vec{r}_i$ is $\vec{P}_i = \alpha_i \vec{E}_{loc,i}$, where $\vec{E}_{loc,i}$ the sum of the incident plane wave field ($\vec{E}_{inc,I}$, retardation effects included) and the contribution from all other N-1 dipoles ($\vec{E}_{dipole,i}$):

$$\vec{E}_{loc,i} = \vec{E}_{inc,i} + \vec{E}_{dipole,i} = \vec{E}_0 \exp\left(i\vec{k}\cdot\vec{r}_i\right) - \sum_{j=1,j\neq i}^{N} \mathbf{A}_{ij}\cdot\vec{P}_j \qquad (11)$$

where $\left|\vec{E}_0\right|$ is the amplitude of the incident wave and k = ω/c. The diploe interaction matrix $\mathbf{A}_{ij}$ is a 3 by 3 matrix. The dipole interaction term has the form:

$$\mathbf{A}_{ij}\cdot\vec{P}_j = \frac{\exp\left(ikr_{ij}\right)}{{r_{ij}}^3}\left\{k^2\vec{r}_{ij}\times\left(\vec{r}_{ij}\times\vec{P}_j\right) + \frac{\left(1-ikr_{ij}\right)}{{r_{ij}}^2}\times\left[{r_{ij}}^2\vec{P}_j - 3\vec{r}_{ij}\left(\vec{r}_{ij}\cdot\vec{P}_j\right)\right]\right\}\ (j\neq i) \qquad (12)$$

where $\vec{r}_{ij}$ is the vector from dipole i to j and r_{ij} is the magnitude of that vector. $\vec{P}_i$'s are obtained by solving a system of 3N complex linear equations in the form specified as follows, with $\mathbf{A}_{ii} \equiv \alpha_i^{-1}$:

$$\sum_{j=1}^{N} \mathbf{A}_{\mathrm{ij}} \cdot \vec{\mathrm{P}}_{\mathrm{j}} = \vec{\mathrm{E}}_{\mathrm{inc,i}} \tag{13}$$

The scattering and extinction cross sections can subsequently be calculated once $\vec{\mathrm{P}}_{\mathrm{i}}$'s are known. DDA methods is only valid when the defined lattice spacing d is small compared to the incident wavelength so that $|\mathrm{n}|\mathrm{kd} \leq 1$, where n is the refractive index of the particles; and d is small enough so that N is large enough to describe the particle shape satisfactorily. When $|\mathrm{n}| \gg 1$, DDA can also fail even if the above validity criteria are satisfied.

2.2 Total Internal Reflection (TIR) and Evanescent Field

The concept of TIR is essential to understanding planar (also called slab) waveguides. Consider an interface separating the region of higher refractive index (n_1) from that of lower refractive index (n_2). When a beam of monochromatic light (plane electromagnetic wave) with wave vector $\vec{k}_i$ impinges on the interface, it splits into a transmitted wave with wave vector $\vec{k}_t$ and a reflected wave with wave vector $\vec{k}_r$ (Fig. 1).

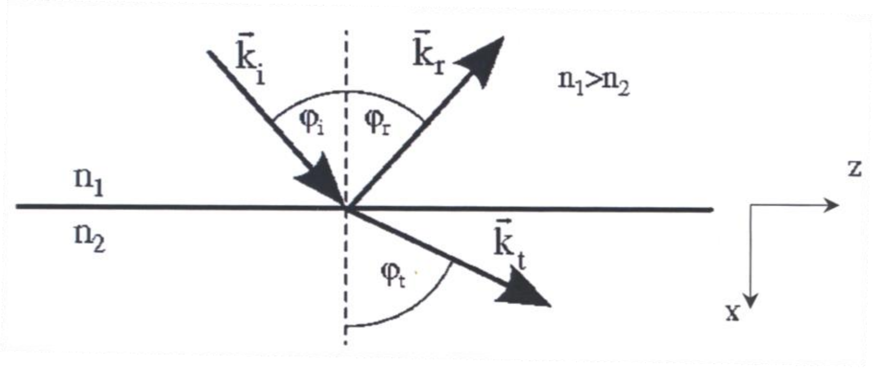

Figure 1. Incident beam is reflected and transmitted at a dielectric interface. Reproduced with permission from [60].

Since all three waves are plane waves, they can be described in the same form with proper subscripts (i, t, r) on $\vec{\mathrm{E}}$, $\vec{\mathrm{E}}_0$, and $\vec{\mathrm{k}}$:

$$\vec{E}(\vec{r},t) = \vec{E}_0 \cdot e^{j(\vec{k}\vec{r}-\omega t)} \tag{14}$$

where $\vec{E}_0$ is the amplitude, j is the imaginary unit ($j = \sqrt{-1}$), $\vec{r}$ is the position vector, ω is the angular frequency, and t is the time. The transmitted wave vector can be expressed as:

$$\vec{k}_t = k_t \begin{pmatrix} \cos\varphi_t \\ 0 \\ \sin\varphi_t \end{pmatrix} = \begin{pmatrix} \sqrt{(\frac{2\pi}{\lambda_0} n_2)^2 - {k_z}^2} \\ 0 \\ k_z \end{pmatrix} \tag{15}$$

$$k_z = \frac{2\pi}{\lambda_0} n_2 \sin(\varphi_t) = \frac{2\pi}{\lambda_0} n_1 \sin(\varphi_i) \tag{16}$$

When the incident angle φ_i is greater than the critical angle derived from Snell's Law ($\varphi_c = \arcsin(n_2/n_1)$), TIR occurs and k_x becomes an imaginary number. A new expression is presented below to account for this change:

$$\vec{k}_t = \begin{pmatrix} j\sqrt{{k_z}^2 - (\frac{2\pi}{\lambda_0} n_2)^2} \\ 0 \\ k_z \end{pmatrix} \tag{17}$$

Inserting equation 17 into 14, we get the general expression for the transmitted wave when the incident angle is greater than the critical angle:

$$\vec{E}(\vec{r},t) = \vec{E}_0 \cdot e^{-\sqrt{{k_z}^2 - (\frac{2\pi}{\lambda_0} n_2)^2} \cdot x} \cdot e^{j k_z \cdot z} \cdot e^{-j\omega t} \tag{18}$$

It can be seen that the transmitted wave propagates along the z-direction and decays exponentially along the x-direction. The field produced by the exponentially decaying component is thus evanescent.

2.3 Planar Waveguides

The principles of guided optical waves will be discussed in this section in the context of a planar waveguide. Consider a three-layer planar waveguide (Fig. 2) with refractive index

n_s for the substrate layer, n_f for the waveguiding layer (thin film), and n_c for the cover. n_f needs to be greater than other two to guarantee TIR at the interfaces. The cover does not need to be a solid. In this thesis, it is either air or a liquid.

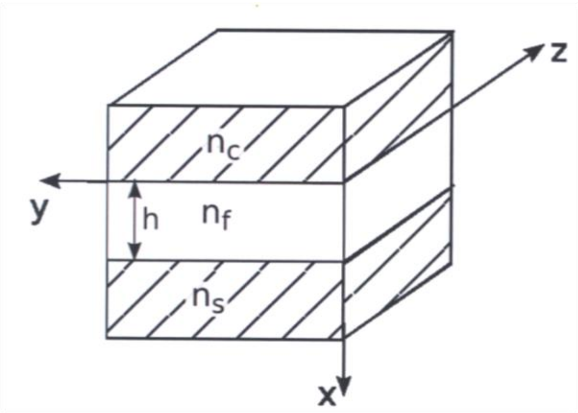

Figure 2. Schematic sketch of a three-layer planar waveguide. Reproduced with permission from [60].

Ray optics approach is used. Imagine a beam propagating in the film layer which gets reflected total internally on the film-cover and film-substrate interfaces, with incident angle φ (> φ_c). A phase shift will occur at each interface depending on the incident angle and polarization of the incoming beam. For s-polarized light, the incident electric field oscillates along the y-direction. The resulted phase shifts (ϕ) at the two interfaces can be obtained from Fresnel equations:

$$\tan\phi_{f,s} = \frac{\sqrt{n_f{}^2 \sin\varphi - n_s{}^2}}{n_f \cos\varphi} \tag{19}$$

$$\tan\phi_{f,c} = \frac{\sqrt{n_f{}^2 \sin\varphi - n_c{}^2}}{n_f \cos\varphi} \tag{20}$$

The resulted phase shifts for p-polarized light whose electric field oscillates along the x-direction can be calculated in a similar way:

$$\tan\phi_{f,s} = \frac{n_f{}^2}{n_s{}^2}\frac{\sqrt{n_f{}^2 \sin\varphi - n_s{}^2}}{n_f \cos\varphi} \tag{21}$$

$$\tan\phi_{f,c} = \frac{n_f{}^2}{n_c{}^2}\frac{\sqrt{n_f{}^2\sin\varphi - n_c{}^2}}{n_f\cos\varphi} \tag{22}$$

For each polarization, a guided mode is only possible when the two reflected waves interfere constructively, which means the overall phase shift has to be multiples of 2π:

$$2hk_0n_f\cos\varphi - 2\phi_{f,s} - 2\phi_{f,c} = 2\pi q \tag{23}$$

where h is the thickness of the film, k_0 is the incident wave vector in vacuum, and q = 1, 2, 3… Equation 23 can be used to calculate the number of guided modes in a given waveguide. A guided mode is manifested as a propagating standing wave along the z-direction with a field distribution along the x-direction that is specific to the polarization, the incident angle, the thickness and refractive index of each layer within the waveguide. As can be observed from Fig. 3, the mode profile is sinusoidal within the waveguide and exponential extending into the substrate or the cover. The mode number (m) corresponds to the number of times a mode profile intersects with x-axis. For example, TE_0 mode does not cross the x-axis whereas TE_1 mode crosses once. Each mode has a unique propagation velocity which is defined as the effective refractive index: $N_{eff} = n_f\sin\varphi_m$. φ_m is the incident angle for mode m (TE_m or TM_m). The propagation constant of that specific mode is then defined as $\beta_m = k_0N_{eff.}$

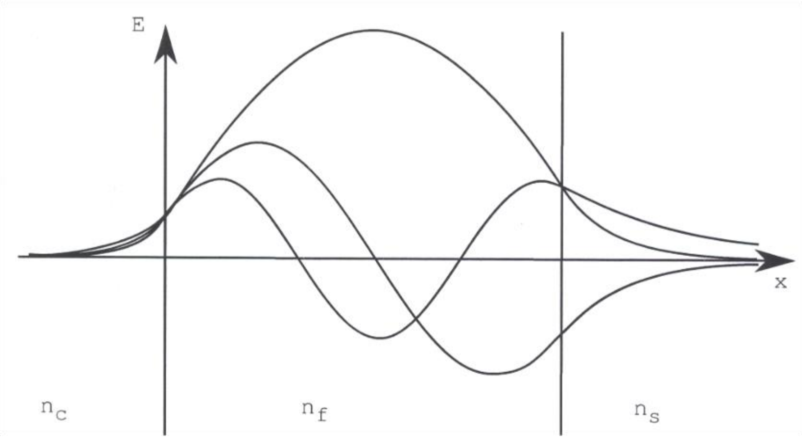

Figure 3. TE_0, TE_1, and TE_2 modes of an asymmetric planar waveguide. $n_c<n_s<n_f$. Reproduced with permission from [60].

2.4 Grating Coupler

Due to its compact design, a grating coupler is used to couple light into waveguides in the work reported in this thesis. Other coupling methods such as end-face coupling, prism coupling and tapered coupling are detailed in [61-62]. In this section, the conditions for the effective coupling of an incident beam to a selected mode is explained.

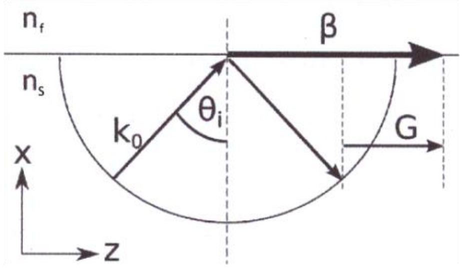

Figure 4. Phase-matching in a grating coupler. Reproduced with permission from [60].

The coupling occurs when the wave vectors of the incident light and the mode match. The coupling condition can be written as:

$$\beta_m = \beta_i \pm G = n_s k_0 \sin\varphi_i \pm\ o\frac{2\pi}{d} \tag{24}$$

where φ_i is the incident angle, o (= 0, 1, 2…) is the diffraction order, d is the periodicity of the diffraction grating. We can see that the propagation constant of the incident light needs to be boosted by the grating vector G. The propagation constants and the grating vector are directional, but are written in their scalar forms for the sake of simplicity.

2.5 References

46. Kreibig, U.; Vollmer, M., *Optical properties of metal clusters*. Springer: 1995.

47. Anatoliy, P.; Gero von, P.; Uwe, K., Influence of interband electronic transitions on the optical absorption in metallic nanoparticles. *Journal of Physics D: Applied Physics* **2004,** *37* (22), 3133.

48. Bassani, G. F.; Parravicini, G. P., *Electronic states and optical transitions in solids*. Pergamon Press: 1975.

49. Mie, G., Beiträge zur Optik trüber Medien, speziell kolloidaler Metallösungen. *Annalen der Physik* **1908,** *330* (3), 377-445.

50. Bohren, C. F.; Huffman, D. R., *Absorption and scattering of light by small particles*. Wiley: 1983.

51. Abramowitz, M., *Handbook of Mathematical Functions, With Formulas, Graphs, and Mathematical Tables*. Dover Publications, Incorporated: 1974.

52. Hergert, W.; Wriedt, T., *The Mie Theory: Basics and Applications*. Springer Berlin Heidelberg: 2012.

53. Draine, B. T.; Flatau, P. J., Discrete-Dipole Approximation For Scattering Calculations. *Journal of the Optical Society of America A* **1994,** *11* (4), 1491-1499.

54. Zhao, J.; Pinchuk, A. O.; McMahon, J. M.; Li, S.; Ausman, L. K.; Atkinson, A. L.; Schatz, G. C., Methods for Describing the Electromagnetic Properties of Silver and Gold Nanoparticles. *Accounts of Chemical Research* **2008,** *41* (12), 1710-1720.

55. Jensen, T.; Kelly, L.; Lazarides, A.; Schatz, G. C., Electrodynamics of Noble Metal Nanoparticles and Nanoparticle Clusters. *Journal of Cluster Science* **1999,** *10* (2), 295-317.

56. Purcell, E.; Pennypacker, C., Scattering and Absorption of Light by Nonspherical Dielectric Grains. *The Astrophysical Journal* **1973,** *186*, 705.

57. Jin, J. M., *The Finite Element Method in Electromagnetics*. Wiley: 2014.

58. Kane, Y., Numerical solution of initial boundary value problems involving maxwell's equations in isotropic media. *IEEE Transactions on Antennas and Propagation* **1966,** *14* (3), 302-307.

59. Martin, O. J. F.; Girard, C.; Dereux, A., Generalized Field Propagator for Electromagnetic Scattering and Light Confinement. *Physical Review Letters* **1995,** *74* (4), 526-529.

60. Nitsche, M. Setting up a microscopy workplace for evanescent fluorescent waveguide microscopy on biological tissue. RheinMain University of Applied Sciences, Rüsselsheim, 2007.

3 A Mass-Producible and Versatile Sensing System: Localized Surface Plasmon Resonance Excited by Individual Waveguide Modes [63]

This chapter is reprinted with permission from Ding, Z., Stubbs, J., McRae, D., Blacquiere, J., Lagugné-Labarthet, F., Mittler, S., *A Mass-Producible and Versatile Sensing System: Localized Surface Plasmon Resonance Excited by Individual Waveguide Modes.* ACS Sensors, 2018. **3**(2): p. 334-341. Copyright 2018 American Chemical Society. The copyright permission is included in Appendix A.

Abstract: A plasmonic sensing system that allows the excitation of localized surface plasmon resonance (LSPR) by individual waveguide modes is presented conceptually and experimentally. Any change in the local environment of the gold nanoparticles (AuNPs) alters the degree of coupling between LSPR and a polymer slab waveguide, which then modulates the transmission-output signal. In comparison to conventional LSPR sensors, this system is less susceptible to optical noise and positional variation of signals. Moreover, it enables more freedom in the exploitation of plasmonic hot spots with both transverse electric (TE) and transverse magnetic (TM) modes. Through real-time measurement, it is demonstrated that the current sensing system is more sensitive than comparable optical fiber plasmonic sensors. The highest normalized bulk sensitivity (7.744 RIU^{-1}) is found in the TM_1 mode. Biosensing with the biotin-streptavidin system shows that the detection limit is on the order of 10^{-14} M for streptavidin. With further optimization, this sensing system can easily be mass-produced and incorporated into high throughput screening devices, detecting a variety of chemical and biological analytes via immobilization of the appropriate recognition sites.

3.1 Introduction

Localized surface plasmon resonance (LSPR) sensors spark intensive research due to their potential applications in disease diagnosis, drug discovery [64], proteomics [65], and environmental detection [66]. Gold nanoparticles (AuNPs) exhibit LSPR when the incident photon frequency matches the oscillation frequency of conduction electrons [23]. The resonance results in a strong UV-Vis absorption band whose frequency is highly dependent on the size, shape, distribution, dielectric properties, and local environment of the AuNPs [1]. This frequency sensitivity towards local refractive index enables the transduction of binding events on the AuNPs into optical signals: changes in LSPR resonance wavelength, extinction, or both [23, 67].

The incorporation of a waveguide into LSPR sensor system for absorption-based measurement overcomes four limitations of a conventional plasmonic sensor that works in the direct transmission mode. First, the traditional configurations are susceptible to optical noise introduced by irrelevant molecules that scatter or absorb as light propagates [33, 68]. Waveguides, on the other hand, guide light with low loss and are relatively immune to outside interferences. Second, positional variation of signals resulting from the nonuniform and polydisperse nature of the nanoparticle population compromises the reproducibility of sensor behaviour. In contrast, waveguide sensors detect the integral behaviour of all the nanoparticles inside a sensing area, leading to a higher reproducibility. Third, due to the spectroscopic nature of conventional sensors, bulky prims and moving optical components present engineering challenges for high throughput screening applications [69]. On the contrary, a system of slab waveguide combined with a monochromatic light source is structurally robust and highly miniaturizable [70]. Lastly, transmission-based sensors limit the exploitation of nonspherical plasmonic features that are sensitive to polarized light because the electric field of incident light cannot oscillate in its direction of propagation. The use of a waveguide liberates this limitation.

Herein, conceptually and experimentally, a mass-producible and versatile plasmonic sensing system that allows the excitation of LSPR by individual waveguide modes is presented. This system can be adapted by research groups working on plasmonic nanoparticles of various shapes and sizes, and is able to detect a variety of chemical and biological analytes by immobilizing the appropriate recognition sites on the nanoparticles. To demonstrate the advantages of the system, the mode-specific bulk sensitivity of pancake shaped AuNPs immobilized onto the waveguide surface via organometallic chemical vapor deposition (OMCVD) is studied. First, the quality of the slab waveguide before and after gold deposition is characterized via m-line spectroscopy.

Through real-time measurement, it is demonstrated that the current sensing system is more sensitive than comparable optical fiber plasmonic sensors [71-72]. Furthermore, optimization strategies in the context of the sensitivity study are discussed.

3.2 Experimental Section

3.2.1 Materials

Chloro(trimethylphosphine)gold(I) (99%), methyl lithium (1.6 M in diethyl ether), lithium aluminum hydride (95%), magnesium sulfate, chlorobenzene, trichloro(octadecyl)silane (OTS), 11-mercapto-1-undecanol (97%; referred to as alkane thiol hereafter), and silicon sheets were acquired from Sigma Aldrich (Ontario, Canada). Sulfuric acid (98%), hydrogen peroxide (30%), ethanol, glycerol, and toluene were obtained from Caledon Laboratories Ltd. (Ontario, Canada). Polystyrene granules were purchased from Goodfellow Cambridge Ltd. (Huntingdon, England). Monothiolalkane PEG-biotin was purchased from SensoPath Technologies (Montana, USA). Streptavidin was obtained from Rocklan Immunochemicals Inc. (Pennsylvania, USA). Diethyl ether was distilled from lithium aluminum hydride and degassed before use. Water used during this study was deionized, obtained from Millipore cartridges. All other materials were used without further purification. Fused silica substrates with a coupling grating (2.5 cm × 5 cm, 1 cm between the top and the grating edge) were fabricated at the RheinMain University of Applied Sciences Wiesbaden, Rüsselsheim, Germany. OMCVD was carried out in a custom-made glass chamber.

3.2.2 OMCVD

Methyl(trimethylphosphine)gold(I) was synthesized as previously described in the literature [73]. AuNPs were deposited as previously described with modifications [73]. Information regarding the instrumentation (spin coater and UV ozone generator) is documented in the same paper [73]. Fused silica substrates carrying a coupling grating were used as waveguide substrates. The spin coating solution was prepared by dissolving 1.5 g of polystyrene in 13 mL of chlorobenzene. The spin coating speed for the polystyrene waveguide was 2200 rpm. The baking process after spin coating was omitted. A piece of silicon sheet, the same size as the waveguide, with a circle carved out (1.6 cm in diameter, 1.5 cm away from the top), was placed on top of the polystyrene waveguide during UV ozone treatment. Additionally, 0.6 mL of hydrogen peroxide was added into the UV ozone chamber to enhance -OH group creation on the polystyrene waveguide. OMCVD was performed at 65.5 °C for 11 min 30 s under 13.5 Pa.

3.2.3 Optical Setup and UV-Vis Spectroscopy

Modified from the literature [74], the optical setup of m-line spectroscopy and bulk sensing is essentially the same. Light emitted from a red HeNe laser (632.8 nm, 10 mW; JDS Uniphase, USA) passes through an optical chopper (Signal Recovery 197, Ametek Inc. USA), a linear polarizer (Newport Corporation, USA), and an iris (Thorlabs ID8, USA) before reaching the edge of the coupling grating. Waveguide transmission is measured with a photodiode pressed against its end face. The photodiode signal is modulated by a lock-in amplifier (Signal Recovery 7265 DSP) for noise reduction. A sample holder, clamping the waveguide and a Teflon® flow cell (1 mL) in place, is situated on a three-axis mount (Owis, Germany), which is controlled by a goniometer (Huber, Model 414, Germany). Both the goniometer and the lock-in amplifier are connected to a computer. All optical experiments were carried out at 20 °C. The m-line spectrometer was scanned in increments of 0.025°. The angle of incidence is defined as the angle between the incident light and the surface normal (y-axis of Fig. 5.). Coupling angles for individual modes are found at angles with the highest intensities at end face. A software package (MPI for Polymer Research, Mainz, Germany) is used to control the m-line setup. It has two operation modes: a) an m-line mode where the waveguide transmission is measured as a function of incident angle, and b) a kinetic mode where the signal at the end face is measured over time at a fixed coupling angle position. UV-Vis spectroscopy in transmission (perpendicular to the propagation direction of waveguide modes, along y-direction of Fig. 5) was performed with a Lambda 850 UV-Vis spectrometer (Perkin Elmer, USA) to gain information about the spectral response of the AuNPs.

3.2.4 Bulk Sensing

Bulk sensing was carried out in the kinetic mode at the coupling angles obtained from m-line spectroscopy. Starting with water, 2%, 4%, 5%, 7%, 9%, 11%, and 13% of glycerol solutions (by weight) were introduced into the flow cell. The measurement was conducted with TE_0, TE_1, TM_0, and TM_1 waveguide modes. A data point was recorded every 5 s.

3.3 Results and Discussion

3.3.1 Sensing Mechanism and Theoretical Sensitivity

The key elements of the sensing system are illustrated in Fig. 5. Light propagating within the waveguide assumes either a transverse electric (TE, s-polarized light) or a transverse magnetic (TM, p-polarized light) mode. Coupling between the evanescent fields of a waveguide mode and an LSPR mode is contingent upon resonance conditions of the AuNPs being satisfied. Because of this strong coupling, light intensity within the waveguide diminishes. Any increase in local refractive index of the AuNPs leads to a redshift of their extinction peak. Consequently, the coupling is attenuated, and the waveguide transmission signal rebounds. Since scattering behaviour of the AuNPs does not contribute substantially to waveguide transmission, we will simplify the situation by considering absorption spectra only.

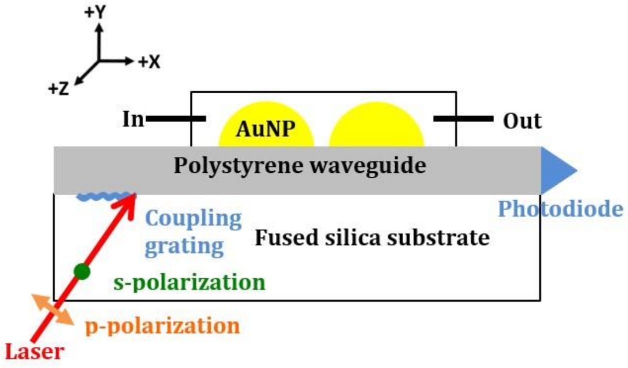

Figure 5. Schematic of the waveguide sensor. A substrate (white) carrying a coupling grating (blue) supports a polystyrene waveguide (grey) with AuNPs (yellow) covalently

bound on top. A flow cell is fixed to cover a circular sensing area where AuNPs are deposited. Mode-selective coupling is conducted outside the flow cell to ensure constant coupling conditions. The intensity of a transmitted waveguide mode is detected by a photodiode (blue triangle) at its end-face. The electrical field oscillates in the xy-plane for p-polarization (orange double arrow), and along the z-axis for s-polarization (green dot).

The bulk sensitivity of the system is defined as the change of signal output divided by the change in refractive index, normalized by the signal of water (or any blank defined by the user). All the liquid media mentioned in this chapter are assumed to be free of charge, homogeneous, and isotropic. Consider a hypothetical absorption spectrum of AuNPs in water described by function A(λ). When a liquid of higher refractive index is introduced, the absorption curve exhibits a redshift of Δλ nm as indicated by the horizontal arrow in Fig. 6. If the increase in refractive index is small enough, we can assume that the resulting absorption spectrum is a redshifted version of the original one. The definition of “small” is specific to the size, shape, distribution, and dielectric environment of AuNPs. Thus, the shifted spectrum can be described by function A(λ- Δλ). We can then approximate A(λ-Δλ) in terms of A(λ) using Taylor expansion, where D' is the first derivative of absorption with respect to wavelength, D'' is the second, and so on.

$$\mathrm{A}(\lambda-\Delta\lambda)=\mathrm{A}(\lambda)-\ \Delta\lambda\mathrm{D}'+\frac{(\Delta\lambda)^2}{2}\mathrm{D}''-\ \frac{(\Delta\lambda)^3}{6}\mathrm{D}'''+\cdots \tag{25}$$

Since the coupling conditions are unaltered throughout the experiment, the sensing area has a constant feed of input intensity. The transmission signal increase with respect to water (ΔI) upon injection of another liquid with a higher refractive index (Δn) is simply the negative of the difference between A(λ) and A(λ-Δλ) at the observation wavelength as marked by the vertical arrow in Fig. 6.

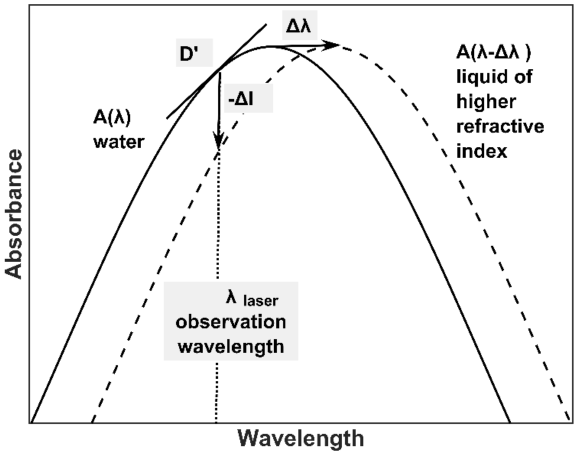

Figure 6. A hypothetical redshift of an absorption spectrum of AuNPs induced by a change in bulk refractive index, Δn. A(λ): spectrum in water, solid curve; A(λ-Δλ): spectrum in a liquid of higher refractive index, dashed curve; ΔI at the observation wavelength, vertical arrow; Δλ, horizontal arrow.

When the redshift is small enough, we can approximate the signal increase with only the first term. Note that the first derivative of absorbance with respect to wavelength (D′) evaluated at the observation wavelength is a constant for a given spectrum. The unit of D' is a.u./nm. Because the LSPR peak wavelength is approximately linear with respect to refractive index (n_i) within a certain range [1], we can decompose Δλ using two proportionality constants, $S_{wavelength}$ and R. $S_{wavelength}$ is the sensitivity of LSPR peak wavelength in nm/RIU. R is the response constant of the photodiode (or other detectors) in mV/a.u. According to the definition earlier, the theoretical bulk sensitivity of this absorption-based system, S_{abs}, within a linear range in RIU^{-1} is:

$$S_{abs} = \frac{I_{liquid} - I_{water}}{\Delta n \times I_{water}} = \frac{D' S_{wavelength} R}{I_{water}} \tag{26}$$

Conventionally, the bulk sensitivity of an LSPR sensor is defined as the rate of wavelength shift versus refractive index change, normalized by the full width of half maximum (FWHM) of the resonance peak ($S_{wavelength}$/FWHM in RIU^{-1}) [75]. A narrow ensemble peak entails rigorous control in AuNP's synthetic techniques, which is necessary to improve the wavelength sensitivity. On the other hand, the sensitivity of this proposed system is independent of FWHM and is amplified by the slope term (D').

3.3.2 Characterization of AuNPs

Polystyrene, like most polymers, is inert towards surface functionalization unless treated with harsh chemicals. Such treatments undermine the integrity and high transparency of polymer waveguides. In comparison, UV-activated ozone is relatively mild and suitable for mass production. Reactive gaseous species generated by the photolysis of ozone react with the polystyrene surface, introducing surface hydroxyl groups through the combination of hydroxyl and carbon radicals [76]. These hydroxyl groups are nucleation sites for Au(0) nanoparticles that are formed through successive bimolecular reductive elimination reactions between monoalkyl Au(I) species [77-78].

However, UV ozone treatment alone did not guarantee a successful gold deposition every time. There were instances where methyl(trimethylphosphine)gold(I) simply re-condensed inside the reaction chamber and no AuNPs were observed at all. The addition of hydrogen peroxide during UV ozone treatment significantly increases the success rate of gold deposition to almost 100%. This might result from an increased surface density of hydroxyl groups, which facilitates the transfer of methyl group from one methyl gold to an adjacent gold center [79].

The LSPR peak wavelength shifts by 10 nm as the bulk refractive index increases from 1.333 to 1.361 (Fig. 7A). The resonance wavelength is significantly redshifted in comparison to colloidal AuNPs of similar size because of the substrate effect [80] and possibly the interaction between gold and hydroxyl groups. Since the shape of the absorption curve does not change significantly, we expect the linear range of sensor performance is approximately between 1.333 and 1.361. The shoulder around 575 nm might be the quadrupole peak that is exposed after the dipolar peak is redshifted [55]. The second peak in the 700 nm regime results from the plasmonic coupling of adjacent nanoparticles [81-82]. The spectra were only taken between 500 and 800 nm to focus on the plasmon peaks.

The diameter distribution (Fig. 7B) of the AuNPs was measured with a scanning electron microscope (SEM; Leo 1540 XB, Carl Zeiss, Oberkochen, Germany). 15 nm of aluminum was sputtered on the polystyrene surface before the AuNPs were studied under 20 kV beam in back-scatter mode (Fig. 7C). The zoomed inset reveals the presence of some clusters, which could result either from melting of the polymer substrate during electron bombardment or from the aluminum deposition process. The mean diameter of the AuNPs was found to be 19 ± 1 nm. The particles smaller than 14 nm were excluded when calculating the mean diameter because they most likely resulted from the inappropriate post-measurement image processing.

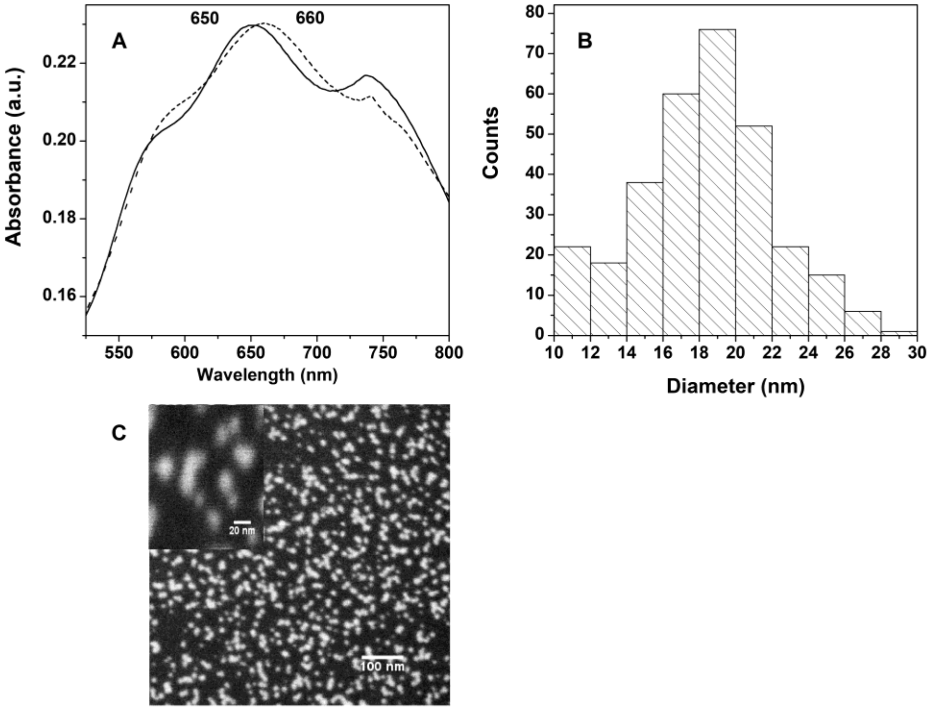

Figure 7. (A) UV-Vis absorption spectra of AuNPs in water (solid) and ethanol (dashed) measured in transmission (along y-axis of Fig. 5). (B) Histogram of particle diameters from SEM image. (C) SEM image of OMCVD AuNPs on polystyrene: large scale bar 100 nm, small scale bar 20 nm. These images are of low quality because a short integration time was used due to the unstableness of the polystyrene substrate. High-

resolution images require a relatively long integration time, which damages the polymer substrate due to electron bombardment and local heating.

The topography of the AuNPs was analyzed with an atomic force microscope (AFM; NanoWizard II, JPK Instruments Inc.) in non-contact mode with 512 × 512 points per image. Commercial silicon tips (NCL-50, NanoWorld Inc.), with resonance frequency of 190 kHz and force constant of 48 N/m, were used in the measurements. The images were processed by taking cross-sections of particles, then determining the height. The average height of 50 particles investigated was found to be 7 ± 3 nm. We therefore deal with pancake shaped AuNPs with an aspect ratio (height/lateral) of 7:19. This finding is consistent with previous studies on OMCVD grown AuNPs with the same precursor. Although a different substrate functionalizing self-assembled monolayer (-SH instead of -OH) was used, the general outline of those AuNPs was found to be pancake shaped as well with aspect ratios (height/lateral) of 1/1.5, 1/10 and 1/1.4 [81].

3.3.3 Waveguide Mode Profiles Before and After Gold Deposition

M-line spectroscopy scans angle of incidence as a function of waveguide transmission for both polarizations, the maxima of which correspond to the coupling angles for individual modes. These data are typically used to calculate the thickness and refractive index ($n \propto \sqrt{\varepsilon'}$, ε' is the real part of dielectric function) of a waveguide, if the optical data of its substrate and coupling grating are known. In a classic m-line, the area of mode coupling is identical to the rest of the waveguide. The peak width delivers information on the imaginary part (ε'') of the dielectric function ($\varepsilon = \varepsilon' + i\varepsilon''$), thus describes the absorption and scattering features of the waveguide. In our case, characterization of the waveguide after gold deposition (Fig. 8, black line) differs from the classic operation in that coupling is performed outside the area with AuNPs and that waveguide transmission is collected after certain degree of energy transfer to AuNPs. As a result, the peak intensities decrease and the peak widths increase in comparison to the bare waveguide (Fig. 8, grey spectra). Simulations with Fresnel equations for waveguide modes reveal increased peak widths and decreased peak heights with increasing absorpt ion in the system. Therefore three related parameters are considered: coupling angle, peak intensity, and peak width. The coupling angle is directly related to the effective refractive index of a guided mode under its coupling conditions [83].

Because the coupling conditions of individual modes remain unaltered before and after gold deposition, their coupling angles, or as depicted in Fig. 8, their peak positions remain unchanged given the uncertainty in angle measurement is ± 0.025º.

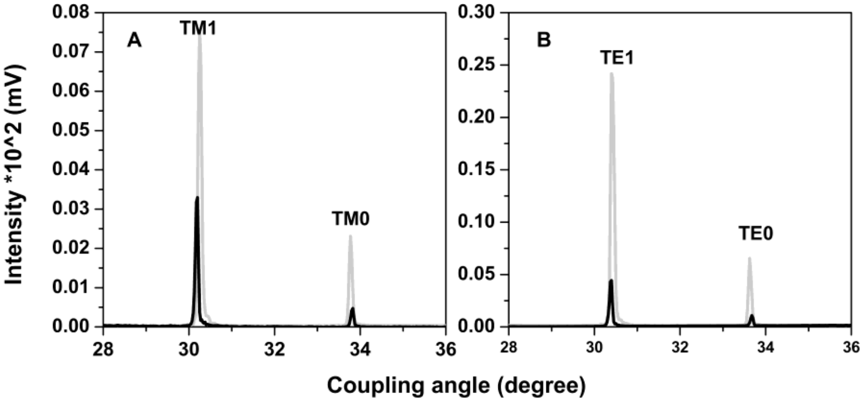

Figure 8. Baseline corrected m-line spectra for (A) p-polarization and (B) s-polarization. Bare waveguide, grey; waveguide after gold deposition, black. Please note the difference in the intensity scale for s- and p-polarization.

To quantify the extent of energy transfer from the waveguide to the AuNPs, we define two normalized parameters: the index of waveguide absorption (IOWA) and the index of nanoparticle absorption (IONA). IOWA = FWHM/I_{max} in (°/mV). IONA = ($IOWA_{AuNP}$ - $IOWA_{bare}$)/$IOWA_{bare}$, which describes the contribution of the AuNPs to coupling peaks measured at the end face. The m-line peaks were fitted with a Gaussian model using Origin Pro 8, from which values of FWHM were extracted. Table 1 summarizes the two parameters for all four guided modes. A more exhaustive table on the parameters of the coupling peaks can be found in Table S1 of Appendix B, together with their experimental errors. The peak intensity, I_{max}, is the value displayed on the lock-in amplifier when the waveguide is turned to the coupling angle of a certain mode.

IONA signifies the normalized proportion of guided light absorbed by AuNPs. The difference between the two polarizations is caused by the distinct absorption behaviour when pancake shaped AuNPs are illuminated along different axes (see Fig. 5 for the coordinate system), which ultimately stems from their unsymmetrical shape and dielectric environment. TE modes probe along the z-axis or the long axes of the pancake shaped AuNPs, whereas TM modes probe mostly in y-direction or along their short axes (a small x-component is ignored for simplicity) [84]. Because the long axis contains more material than the short axis, the particles illuminated by TE modes absorb more light than those excited by TM modes as confirmed by the IONA values in Table 1. Note that lower IONA values of TM modes do not directly translate to less amount of guided light being absorbed because they are normalized values. However, due to the facts that TM modes carry less light before gold deposition and that less proportion of light is absorbed after gold deposition, we can draw the above connections between AuNP absorption and IONA values of two polarizations.

Table 1. Parameters that quantify the extent of energy transfer from the waveguide to the AuNPs.

		TM_0	TM_1	TE_0	TE_1
Bare waveguide	IOWA (°/mV)	0.053	0.013	0.018	0.0039
After gold deposition	IOWA (°/mV)	0.072	0.027	0.073	0.026
	IONA	0.36	1.0	3.0	5.8

Within both polarization directions, the IONA value for the first mode (TM_1 and TE_1) is higher than the zeroth mode (TM_0 and TE_0). Here, the difference in absorption cross section originates from the evanescent fields of different waveguide modes: with increasing mode number, the integrated mode intensity increases [85]. Consequently, within a chosen polarization, LSPR excited by the higher mode generates a more intense plasmonic evanescent field, which leads to a superior sensitivity as we will see in the next section. However, bulk sensitivities for different polarizations cannot be extrapolated from m-line data because higher absorption does not equate to higher sensitivity (rate of change of absorption with respect to refractive index) when AuNPs are illuminated along different axes. In conclusion, we find from the m-line investigation that coupling condition remains unchanged before and after gold deposition. The argument of a constant input in the theoretical derivation is thus valid. Sharp and defined m-line peaks before and after gold deposition translate to a high-quality waveguide, which ensures its reliable sensing behaviour.

3.3.4 Mode-Specific Bulk Sensitivity

The real-time waveguide transmissions of the TE_0, TE_1, TM_0 and TM_1 modes (at their coupling angles) are depicted in Fig. 9A-D. The mode-specific average waveguide transmissions are tabulated in Table S2. The slopes of the linear regression lines (Fig. 9E) represent the normalized bulk sensitivities for individual modes in RIU^{-1}. Their numerical values are 2.654 for TM_0, 7.744 for TM_1, 1.500 for TE_0, and 2.909 for TE_1. Note that the normalized sensitivity for each mode is calculated using the values in Table S2 divided by the transmission signal for water in that mode.

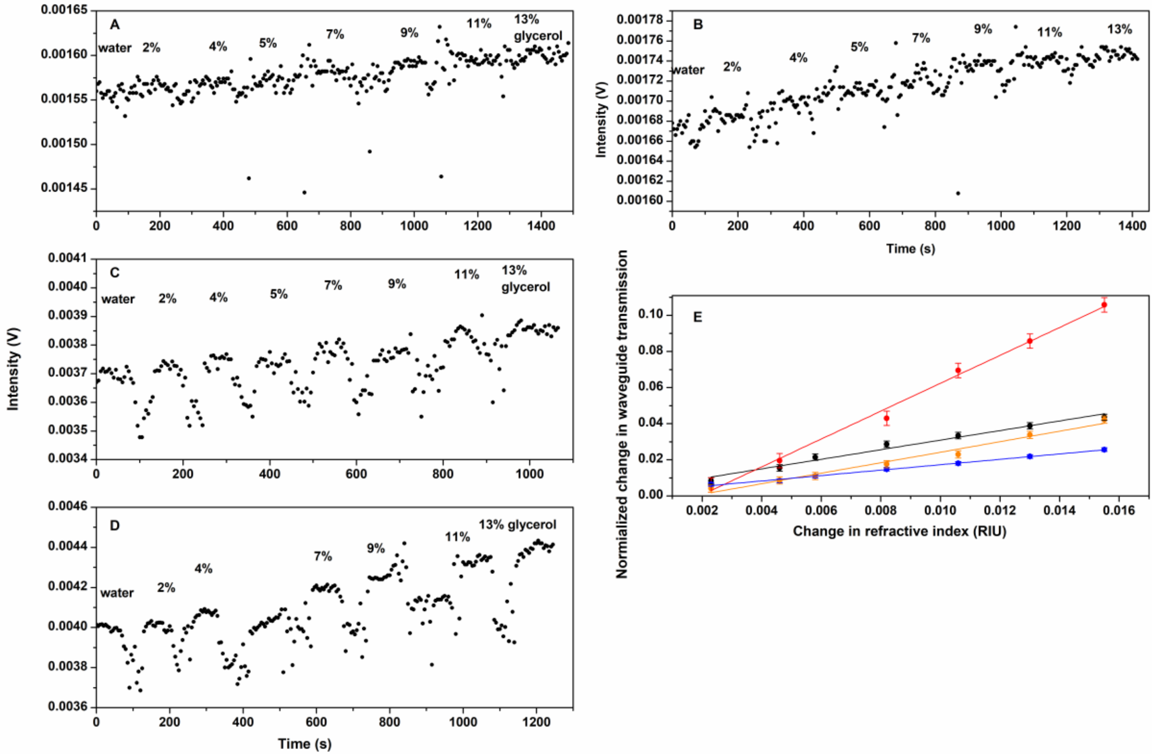

Figure 9. Real-time transmission intensity of the (A) TE$_0$, (B) TM$_0$, (C) TE$_1$, and (D) TM$_1$ mode detected at the waveguide end face. The refractive indices of glycerol solutions: 1.3330, 1.3353, 1.3376, 1.3388, 1.3412, 1.3436, 1.3460, 1.3485 [86]. The uncertainty in intensity measurement is ± 5x10^{-6} V. The periodic oscillation of data points is due to the change of liquids and the elimination of air bubbles. (E) Normalized change in waveguide transmission (unitless) with respect to change in refractive index for TM$_1$ (red), TM$_0$ (black), TE$_1$ (orange), and TE$_0$ (blue). The R^2 values of linear fittings are all above 0.98. Volts instead of mV are shown to keep the original unit and significant figures obtained from measurements.

Although liquid media can absorb or scatter photons while in the evanescent field of the waveguide, they barely contribute to the change in waveguide transmission as the chosen liquids are close to 100% transparent at the observation wavelength of 632.8 nm. Besides, the AuNPs absorb orders of magnitude more photons. The linearity of the signal response for all four modes is not valid beyond a refractive index change of (Δn) 0.0155, with water as the reference. As predicted in the last section, within a chosen polarization direction, S_{bulk} value for the first mode (TM_1 or TE_1) is higher than the zeroth mode (TM_0 or TE_0). This finding aligns with the established fact that integrated mode intensity increases with mode number because other features of the AuNPs are identical within a defined polarization.

LSPR excited by TM modes are more sensitive than that excited by TE modes. Unlike conventional bulk sensing where the dielectric environment is assumed to be homogeneous throughout plasmonic sensing volume; the bulk sensitivity investigated herein is similar to a conventional short distance sensing in that only the absorption caused by AuNPs very close to the waveguide surface is detected and thus contributes to the waveguide transmission at its end face. Both the waveguide and the AuNPs sense by evanescent fields (although of different nature) with exponentially decaying field intensity. Haes et al. studied the short distance sensitivity of immobilized silver nanostructures by functionalizing them with an alkanethiol and measuring the LSPR shift by standard UV-Vis transmission with unpolarized light at 2 nm away from the silver surface [87]. They found that the short distance sensitivity is proportional to out-of-plane height (short axis) and inversely proportional to in-plane length (long axis) of the silver nanostructures. The unpolarized light used in their study is equivalent to the s-polarized light in our study: they both probe along the long axes of plasmonic nanostrucutres that are parallel to the substrate surface. The lower sensitivity of the LSPR induced by TE modes can be attributed to two factors associated with their plasmonic evanescent field: (1) the field intensity decreases due to increased radiative damping effects as the nanoparticle width is increased; (2) the field intensity further decreases due to substrate dielectric effects as larger medium dielectric constants lead to smaller fields [87].

To the best of our knowledge, no LSPR sensing system based on a multimode slab waveguide and a monochromatic light source has been studied. The most comparable sensitivity experiment was carried out using an optical fiber sensor with AuNPs immobilized electrostatically [71] or covalently [72]. Their transmission sensitivities normalized against water were reported to be around one and 4.16 respectively (in RIU^{-1}). Other groups have reported improved sensitivity of 30 and 35 both in a.u./RIU [88-89]. However, the authors did not comment on their choice of the arbitrary absorption unit, nor did they normalize the sensitivity against a blank sample; therefore, their values are not comparable to the ones obtained above. Other than better structural stability, the ease of mode selection of a multimode slab waveguide is preferable over an optical fiber because sensitivity increases with mode number for a defined polarization. Without any rigorous control in the synthetic techniques of the AuNPs, the highest dipolar sensitivity (TM_1 mode) of the sensing system is comparable to the quadrupolar sensitivity of a gold nanobipyramid (7.4 RIU^{-1}) and higher than its dipolar sensitivity (4.5 RIU^{-1}), obtained from wavelength measurement [75].

Biotin-streptavidin system was used to examine the sensor performance (at TM_1 mode) in a biological environment. Thiol solution was prepared in a total concentration of 5×10^{-4} M in ethanol, with 95:5 (molar ratio) of alkane thiol to biotinylated thiol. AuNPs were functionalized with an excess of thiol solution for 12 h. The sensor was exposed to water for a few minutes before the injection of streptavidin to obtain the blank signal. The lowest concentration that leads to a signal increase of more than three times the noise for a blank measurement is 10^{-14} M. Indeed, the injection of 10^{-15} M streptavidin solution did not give rise to a detectable signal. Thus, the limit of detection (LOD) for this sensing system is on the order of 10^{-14} M, which falls on the lower end of the range for LSPR biosensors [22-23, 25]. Without any optimization, this LOD already approaches that for the most sensitive surface plasmon resonance (SPR) sensor [90]. If we assume a linear sensor behaviour, a normalized signal increase of 0.031 (0.083 mV / 2.71 mV) corresponds to a 0.004 increase in refractive index, given that the sensitivity for TM_1 mode is 7.744 RIU^{-1}. As shown in Fig.10, the kinetic signal increases until all streptavidin molecules are bound to biotin, after which the signal plateaus (from 1500 to 2000 s). The observed signal shape is determined by the diffusion of streptavidin molecules as well as the binding kinetics between biotin and streptavidin. Since the signal increases gradually (from 500 to 1500 s) instead of instantaneously as in the bulk sensing experiment, it is not influenced by an increased bulk refractive index introduced by the streptavidin solution.

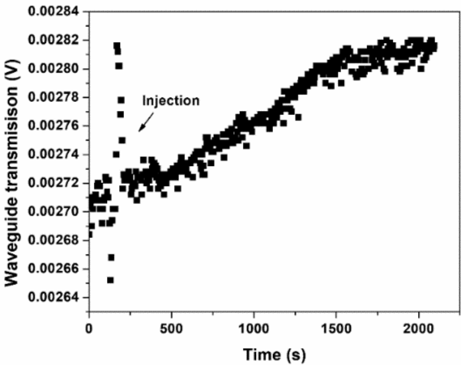

Figure 10. Binding kinetics of streptavidin to biotinylated AuNPs, observed at TM$_1$ mode. The sensor was exposed to water between 0 and 220 s. The streptavidin solution was injected around t = 220 s. The waveguide transmission between 220 and 500 s is slightly higher than that between 0 and 220 s because of an increased bulk refractive index. The blank (water) signal was 2.71 mV. The signal increased by 0.083 mV from 2.725 mV to 2.808 mV.

3.3.5 Factors Affecting the Sensor Performance

We consider three aspects of the sensor performance: sensitivity, stability and reproducibility. The observation wavelength needs to be picked strategically so that the slope of the absorption spectrum is maximized without compromising the reliability, the sensitivity and the linearity of signal response: the steepest section might be too far away from the resonance wavelength, which results in either undetectable signal or signal without a consistent trend. Thanks to the tunability of OMCVD, we have the liberty of testing various AuNP populations with LSPR wavelengths shorter and longer than the observation wavelength (to the shorter and longer wavelength of 632.8 nm). When the absorption maximum falls to the left of the observation wavelength (Fig. 11, red), the observed absorption increases with the redshift of the spectrum, until the LSPR wavelength coincides with the observation wavelength (the red dot to the green dot; a decrease in waveguide transmission). This process is then followed by a further redshift, which leads to a decreased absorption (the green dot to the blue dot) or an increased waveguide transmission. Such inconsistent trend in signal response is undesirable. On the other hand, a sensor with an LSPR wavelength longer than the observation wavelength, such as the system studied here, offers a reliable signal response of increasing waveguide transmission without any reversal (Fig. 6). A certain level of signal fluctuation is expected unless a channel waveguide is implemented; the spreading of light into the z-direction will be not problematic for a micron-wide channel waveguide. Reducing the length of the planar waveguide and increasing the ratio of sensing versus non-sensing area will improve the signal-to-noise ratio, but not significantly.

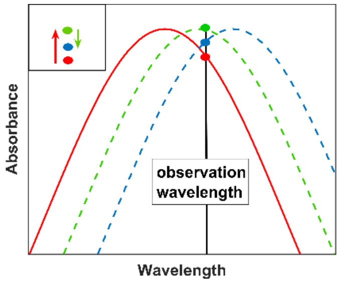

Figure 11. Illustration of the shifting behaviour when the initial LSPR wavelength is below the observation wavelength. The initial absorption spectrum (red) exhibits a redshift (green), then a further shift (blue). The observed absorption at each stage is highlighted with a dot. The change in absorption with the redshift is indicated with arrows in the insert. The time sequence will be red, green, and blue. Such an inconsistent trend is undesirable.

In terms of mechanical stability, a transition from glass substrates to all-polymer substrates will be implemented in the near future, because the latter is much less fragile and more mass-producible. The coupling grating will be hot embossed from a nickel mold. Although the sensor is designed to function as a disposable device, reproducibility still needs to be considered to ensure a consistent sensor performance. One major drawback of OMCVD is the lack of control over the distribution of nanoparticles, which affects both intensity and wavelength sensing. Our signal is rather less affected by a nonuniform distribution because it is determined by the accumulative absorption of all the AuNPs in the path of a propagating mode; whereas conventional wavelength sensing only measures through a single spot. A bulk sensing calibration can be performed to standardize sensor performance by signal offset. Because the linearity of waveguide transmission with respect to refractive index has been confirmed for all four modes, two points should suffice.

3.4 Conclusion

Plasmonic nanoparticles with various shapes and sizes can be covalently immobilized onto the waveguide surface via OMCVD, given the corresponding precursor is available commercially or synthetically. Through an appropriate self-assembled monolayer, the discussed sensing system is able to detect a variety of chemical and biological species. Briefly looking into the future, we expect that with optimization, the sensing system can easily be mass-produced and incorporated into high throughput screening devices.

3.5 References

61. Hunsperger, R. G., *Integrated Optics: Theory and Technology*. Springer New York: 2009.

62. Tamir, T.; Garmire, E., *Integrated optics*. Springer: 1979.

63. Ding, Z.; Stubbs, J. M.; McRae, D.; Blacquiere, J. M.; Lagugné-Labarthet, F.; Mittler, S., A Mass-Producible and Versatile Sensing System: Localized Surface Plasmon Resonance Excited by Individual Waveguide Modes. *ACS Sensors* **2018,** *3* (2), 334-341.

64. Dykman, L. A.; Khlebtsov, N. G., Gold Nanoparticles in Biology and Medicine: Recent Advances and Prospects. *Acta Naturae* **2011,** *3* (2), 34-55.

65. Couto, C.; Vitorino, R.; Daniel-da-Silva, A. L., Gold nanoparticles and bioconjugation: a pathway for proteomic applications. *Critical Reviews in Biotechnology* **2017,** *37* (2), 238-250.

66. Darbha, G. K.; Ray, A.; Ray, P. C., Gold Nanoparticle-Based Miniaturized Nanomaterial Surface Energy Transfer Probe for Rapid and Ultrasensitive Detection of Mercury in Soil, Water, and Fish. *ACS Nano* **2007,** *1* (3), 208-214.

67. Hutter, E.; Fendler, J. H., Exploitation of Localized Surface Plasmon Resonance. *Advanced Materials* **2004,** *16* (19), 1685-1706.

68. Kajiura, M.; Nakanishi, T.; Iida, H.; Takada, H.; Osaka, T., Biosensing by optical waveguide spectroscopy based on localized surface plasmon resonance of gold

nanoparticles used as a probe or as a label. *Journal of Colloid and Interface Science* **2009,** *335* (1), 140-145.

69. Mittler, S., Gold Nanoparticles on Waveguides For and Toward Sensing Application. In *Optical Guided-wave Chemical and Biosensors I*, Zourob, M.; Lakhtakia, A., Eds. Springer Berlin Heidelberg: Berlin, Heidelberg, 2009; pp 209-229.

70. MacCraith, C. S. B. a. L. P. a. B. D., Design and fabrication of enhanced polymer waveguide platforms for absorption-based optical chemical sensors. *Measurement Science and Technology* **2004,** *15* (6), 1140.

71. Chau, L.-K.; Lin, Y.-F.; Cheng, S.-F.; Lin, T.-J., Fiber-optic chemical and biochemical probes based on localized surface plasmon resonance. *Sensors and Actuators B: Chemical* **2006,** *113* (1), 100-105.

72. Lin, H.-Y.; Huang, C.-H.; Cheng, G.-L.; Chen, N.-K.; Chui, H.-C., Tapered optical fiber sensor based on localized surface plasmon resonance. *Optics Express* **2012,** *20* (19), 21693-21701.

73. Kandeepan, S.; Paquette, J. A.; Gilroy, J. B.; Mittler, S., OMCVD Gold Nanoparticles Covalently Attached to Polystyrene for Biosensing Applications. *Chemical Vapor Deposition* **2015,** *21* (10-11-12), 275-280.

74. Lee, T. M.; Mittler-Neher, S.; Neher, D.; Stegeman, G. I.; Roux, C.; Leclerc, M.; Martin, J.; Najafi, S. I., Side-chain dilution effects on the optical properties of poly[3-alkylthiophene]s. *Optical Materials* **1992,** *1* (2), 65-70.

75. Yong, Z.; Lei, D. Y.; Lam, C. H.; Wang, Y., Ultrahigh refractive index sensing performance of plasmonic quadrupole resonances in gold nanoparticles. *Nanoscale Research Letters* **2014,** *9* (1), 187-187.

76. MacManus, L. F.; Walzak, M. J.; McIntyre, N. S., Study of ultraviolet light and ozone surface modification of polypropylene. *Journal of Polymer Science Part A: Polymer Chemistry* **1999,** *37* (14), 2489-2501.

77. Puddephatt, R. J., Reactivity and mechanism in the chemical vapour deposition of late transition metals. *Polyhedron* **1994,** *13* (8), 1233-1243.

78. Tamaki, A.; Kochi, J. K., Formation and decomposition of alkyl-gold(I) complexes. *Journal of Organometallic Chemistry* **1973,** *61*, 441-450.

79. Muhich, C. L.; Qiu, J.; Holder, A. M.; Wu, Y.-C.; Weimer, A. W.; Wei, W. D.; McElwee-White, L.; Musgrave, C. B., Solvent Control of Surface Plasmon-Mediated Chemical Deposition of Au Nanoparticles from Alkylgold Phosphine Complexes. *ACS Applied Materials & Interfaces* **2015,** *7* (24), 13384-13394.

80. Kelly, K. L.; Coronado, E.; Zhao, L. L.; Schatz, G. C., The Optical Properties of Metal Nanoparticles: The Influence of Size, Shape, and Dielectric Environment. *The Journal of Physical Chemistry B* **2003,** *107* (3), 668-677.

81. Aliganga, A. K. A.; Lieberwirth, I.; Glasser, G.; Duwez, A.-S.; Sun, Y.; Mittler, S., Fabrication of equally oriented pancake shaped gold nanoparticles by SAM-templated OMCVD and their optical response. *Organic Electronics* **2007,** *8* (2), 161-174.

82. Rafsanjani, S. M. H.; Cheng, T.; Mittler, S.; Rangan, C., Theoretical proposal for a biosensing approach based on a linear array of immobilized gold nanoparticles. *Journal of Applied Physics* **2010,** *107* (9), 094303.

83. Höök, F.; Vörös, J.; Rodahl, M.; Kurrat, R.; Böni, P.; Ramsden, J. J.; Textor, M.; Spencer, N. D.; Tengvall, P.; Gold, J.; Kasemo, B., A comparative study of protein adsorption on titanium oxide surfaces using in situ ellipsometry, optical waveguide lightmode spectroscopy, and quartz crystal microbalance/dissipation. *Colloids and Surfaces B: Biointerfaces* **2002,** *24* (2), 155-170.

84. Quantum Electronics—Principles and Applications A2 - Marcuse, Dietrich. In *Theory of Dielectric Optical Waveguides (Second Edition)*, Academic Press: 1991; p 381.

85. Thoma, F.; Langbein, U.; Mittler-Neher, S., Waveguide scattering microscopy. *Optics Communications* **1997,** *134* (1), 16-20.

86. Hoyt, L. F., New Table of the Refractive Index of Pure Glycerol at 20°C. *Industrial & Engineering Chemistry* **1934,** *26* (3), 329-332.

87. Haes, A. J.; Zou, S.; Schatz, G. C.; Van Duyne, R. P., Nanoscale Optical Biosensor: Short Range Distance Dependence of the Localized Surface Plasmon Resonance of Noble Metal Nanoparticles. *The Journal of Physical Chemistry B* **2004,** *108* (22), 6961-6968.

88. Sai, V. V. R.; Kundu, T.; Mukherji, S., Novel U-bent fiber optic probe for localized surface plasmon resonance based biosensor. *Biosensors and Bioelectronics* **2009,** *24* (9), 2804-2809.

89. Mitsui, K.; Handa, Y.; Kajikawa, K., Optical fiber affinity biosensor based on localized surface plasmon resonance. *Applied Physics Letters* **2004,** *85* (18), 4231-4233.

90. Zhang, Q.; Jing, L.; Zhang, J.; Ren, Y.; Wang, Y.; Wang, Y.; Wei, T.; Liedberg, B., Surface plasmon resonance sensor for femtomolar detection of testosterone with water-compatible macroporous molecularly imprinted film. *Analytical Biochemistry* **2014,** *463* (Supplement C), 7-14.

4 Narrowing of Plasmon Resonance Peaks as an Ensemble Effect

This chapter contains materials from an accepted manuscript to The Journal of Physical Chemistry C. The manuscript is subject to ongoing editorial changes. The copyright permission from the editor is included in Appendix A.

Abstract: The frequency of localized surface plasmon resonance (LSPR) displayed by gold nanoparticles (AuNPs) redshifts as a function of their local refractive index, which renders them valuable transducers for sensing applications. An ensemble hypothesis is presented herein, along with spectroscopic evidence, using the biotin-streptavidin system on immobilized AuNPs to interpret the decrease in ensemble linewidth (ELW) consistently observed upon functionalization of plasmonic nanoparticles and the subsequent analyte binding. These results demonstrate that ELW can be used to monitor recognition reactions, providing spectral details and a possible sensitivity enhancement to the conventional wavelength sensing. A novel sensing platform allowing the simultaneous measurement of both LSPR wavelength and ELW is proposed, which not only combines the advantages of both parameters but also permits real-time measurement and miniaturization.

4.1 Introduction

Gold nanoparticles (AuNPs) exhibit localized surface plasmon resonance (LSPR) whose frequency is dependent on their size, shape, interparticle spacing, and local environment.[91-92] This latter dependency renders them valuable transducers that convert small changes in the local refractive index into spectral shifts of their extinction spectra.[93-94]

Significant effort has been dedicated to improving the intrinsic sensitivity of LSPR sensors via the optimization of instrumental setups[95-96]; as well as the exploitation of novel geometries[97-99] and materials[100-102] for higher polarizabilities. As an alternative to wavelength and intensity sensing, the sensitivity can be further improved extrinsically by monitoring the change in curvature[27] and inflection points[28] of the resonance peak. These extrinsic methods are post-measurement manipulations of the extinction spectra that require strategic smoothing algorithms so that the signal to noise ratio (S/N) is not degraded by numerical differentiation[103]. Thus, challenges exist if one wishes to obtain real-time results on a portable device that relies on a relatively simple and universal processing algorithm.

To detect a specific analyte, AuNPs typically need to be functionalized with a self-assembled monolayer (SAM), with the corresponding recognition moieties exposed on the outside.[104-105] Spectroscopic measurements[106-107] and theoretical models[108-110] have shown that chemical interface damping induced by adsorbate molecules increases the homogeneous spectral linewidth of a single plasmonic nanoparticle. One could argue that if every single nanoparticle within an ensemble displays the same amount of spectral redshift, the ensemble spectrum should broaden as a summation of individual damping. However, a decrease in the ensemble spectral linewidth is consistently observed for plasmonic nanoparticles, upon both SAM formation and analyte binding (see Table S3 for the estimated peak widths).[27, 37, 111-114] The reason for such narrowing phenomenon has never been discussed.

Herein, an ensemble hypothesis along with experimental evidence is presented as an interpretation of the ensemble narrowing effect, based on which a novel avenue of sensing is proposed using the classic biotin-streptavidin system as a demonstration. This portable sensing platform is highly adaptable and allows the simultaneous register of both LSPR peak position and bandwidth, providing comprehensive spectral information as well as possibilities of extrinsic sensitivity enhancement, real-time measurement and facile miniaturization.

4.2 Experimental Section

4.2.1 Materials

Chloro(trimethylphosphine)gold(I) (99%), methyl lithium (1.6 M in diethyl ether), lithium aluminum hydride (95%), magnesium sulfate, chlorobenzene, trichloro(octadecyl)silane (OTS), and 11-mercapto-1-undecanol (97%; referred to as alkane thiol hereafter) were acquired from Sigma Aldrich (Ontario, Canada). Sulfuric acid (98%), hydrogen peroxide (30%), acetone, ethanol, methanol, 1-propanol, and toluene were obtained from Caledon Laboratories Ltd. (Ontario, Canada). Polystyrene granules and polymethylmethacrylate (PMMA) sheets were obtained from Goodfellow Cambridge Ltd. (Huntingdon, England). Monothiolalkane PEG-biotin was purchased from SensoPath Technologies (Montana, USA; referred to as biotinylated thiol hereafter). Streptavidin was obtained from Rocklan Immunochemicals Inc. (Pennsylvania, USA). Plain microscope slides were purchased from Bio Nuclear Diagnostics Inc. (Ontario, Canada). Diethyl ether was distilled from lithium aluminum hydride and degassed before use. Water used during this study was deionized, obtained from Millipore cartridges. All other materials were used without further purification. Organometallic chemical vapor deposition (OMCVD) was carried out in a custom-made glass chamber.

4.2.2 OMCVD

Methyl(trimethylphosphine)gold(I) was synthesized as previously described in the literature.[73] Gold nanoparticles (AuNPs) were deposited as previously described with modifications.[73] Microscope slides were cut into 0.8 cm by 2.5 cm pieces and cleaned in 1:1 ethanol and acetone mixture by sonication for 30 min before use. Polymer substrate was prepared by spin coating polystyrene solution (1.5 g in 13 mL of chlorobenzene) on pre-cut PMMA (0.8 cm by 2.5 cm) at 2200 rpm. Hydrogen peroxide (1 mL) was added into UV ozone chamber to enhance the creation of surface –OH groups on microscope slides or PMMA substrates. OMCVD was carried out at 65.5 °C under 13 Pa for 6-8 min to yield various sizes of AuNPs.

4.2.3 Scanning Electron Microscopy (SEM) Characterization of AuNPs

The diameter range was determined with an SEM (Leo 1540 XB, Carl Zeiss, Oberkochen, Germany) under 20 kV beam in back-scatter mode. 15 nm of aluminum was sputtered onto substrates prior to measurements. The microscopy images are of low quality due to the non-conducting nature of glass. Four different samples with LSPR peak wavelength of 532.5 nm, 578.0 nm, 552.0 nm and 514.5 nm were measured. Their respective diameters were 6.6 ± 1.2 nm (Fig. 12A), 8.6 ± 1.9 nm (Fig. 12B), 7.4 ± 1.6 nm (Fig. 12C), and 5.6 ± 1.3 nm (Fig. 12D). The sample shown in Fig. 12B was not used for spectral study due to the crowdedness of the nanoparticles. Its size measurement represents the upper limit of the nanoparticles studied. Since the mean diameter increases with LSPR wavelength[115], nanoparticles from all the samples studied fall within the regime of electrostatic approximation.[55]

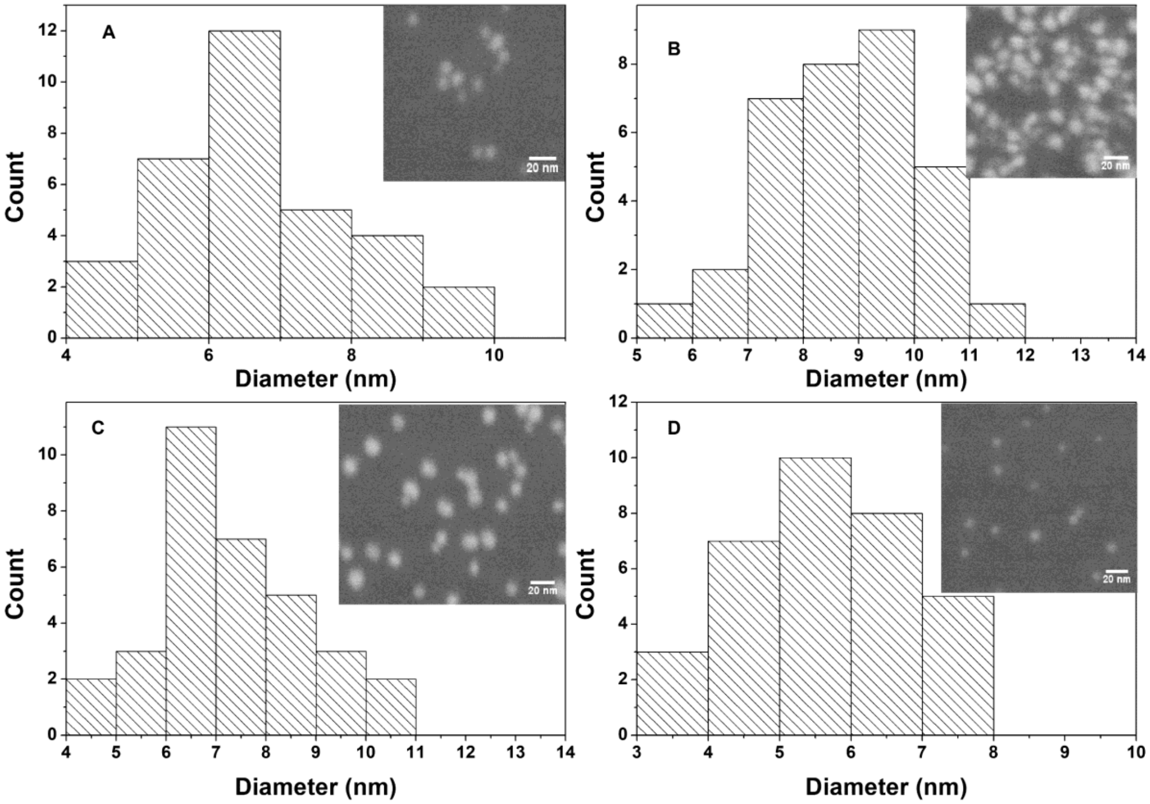

Figure 12. SEM images and diameter distribution of four different ensembles/samples of AuNPs with localized surface plasmon resonance (LSPR) peak wavelength of 532.5 nm (A), 578.0 nm (B), 552.0 nm (C) and 514.5 nm (D). Their respective diameters were 6.6 ± 1.2 nm, 8.6 ± 1.9 nm, 7.4 ± 1.6 nm, and 5.6 ± 1.3 nm. Sample B was measured under SEM as a demonstration of the upper size limit of the nanoparticles studied. It was not used for spectral measurement due to the crowdedness of the nanoparticles.

4.2.4 Biosensing

All absorption spectra were obtained in water for glass substrates and in air for polymer substrates, using a Lambda 850 UV-vis spectrometer (Perkin Elmer, USA) in transmission mode. The scanning was performed between 400 and 800 nm, in increments of 0.5 nm for glass substrates and 2 nm for polymer substrates. The SAM was prepared with 95:5 (molar ratio) of alkane thiol to biotinylated thiol in a total concentration of 5×10^{-4} M ethanolic solution. AuNP samples were functionalized with an excess of thiol solution for 18~24 h. Each sample was exposed to higher and higher concentration of aqueous streptavidin solutions between 10^{-12} and 10^{-5} M. Each concentration was allowed at least 3h reaction time. The samples were rinsed thoroughly with water before taking their spectra to minimize unspecific binding. Bulk sensing was performed in the same configuration.

4.2.5 Calculation of Ensemble Linewidth (ELW)

The ensemble linewidth, ELW, is defined as the spectral distance between the LSPR peak position (λ_0) and the half-maximum position (λ_1) toward the direction of longer wavelengths, such as the red and the blue arrows in Fig. 13. All spectra were corrected for baseline and normalized before ELW was extracted. The baseline was set to be the absorption value at 700 nm from each raw spectrum due to the presence of strong interference pattern from the substrate between 700 and 800 nm. The normalization was performed so that the maximum absorption is unity. The LSPR peak position (λ_0) was the spectral position with the highest absorption value. The half-maximum position (λ_1) was found from actual spectra using an iterative process to select the spectral position whose absorption is closest to 0.5. The above steps were executed using MATLAB 2016.

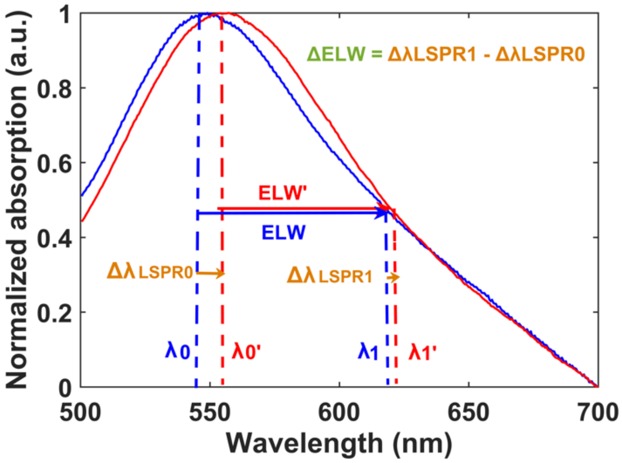

Figure 13. The normalized and baseline corrected absorption spectrum of an ensemble of AuNPs before (blue) and after (red) being functionalized with the mixed thiol SAM. The shift of maximum position ($\lambda_0 \rightarrow \lambda_0'$) and half maximum position ($\lambda_1 \rightarrow \lambda_1'$) determines the values of $\Delta\lambda_{LSPR0}$ and $\Delta\lambda_{LSPR1}$, respectively. The blue and red arrows (ELW and ELW’) are staggered for better visualization.

4.3 Results and Discussion

4.3.1 Premises of the Ensemble Hypothesis and Their Validity

As defined in section 4.2.5, ELW excludes the spectral region on the low-energy side of the resonance peak, so that interband transition near the L-symmetry point with onset energy of 2.4 eV is avoided for its effect on the spectral linewidth of single nanoparticles, thus also on the ELW.[24] Although there is another interband transition near the X-symmetry point with onset energy of 1.8 eV, its absorption cross section is much weaker in comparison to the L-symmetry transition.[116-118] Thus, the X-symmetry interband transition has negligible contribution to the ELW. This argument can also be supported experimentally, where surface-immobilized AuNPs were exposed to two different bulk refractive indices (Fig. 14A). The ELW stayed constant within measurement uncertainty even though the reversible shift of the plasmon peak altered the spectral overlap between the X-symmetry transition edge and the LSPR peak position.

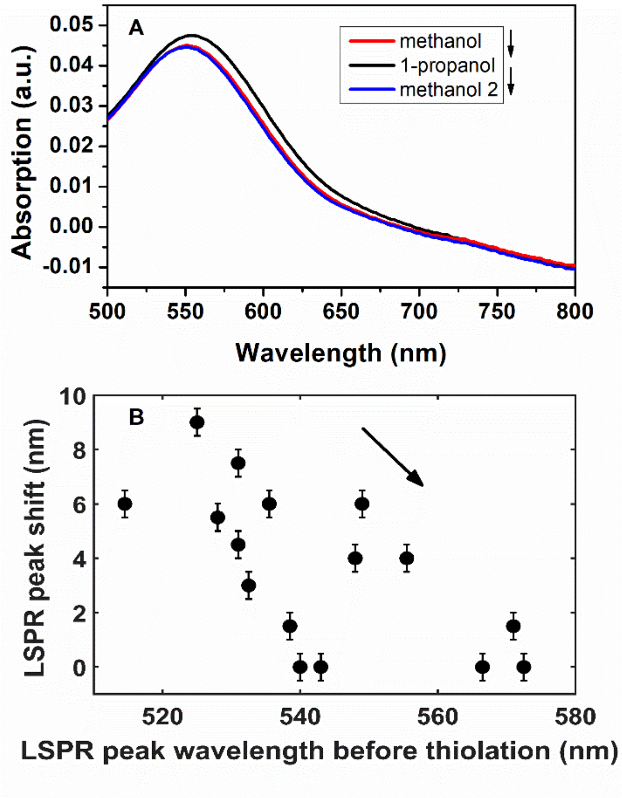

Figure 14. (A) The raw absorption spectra of surface-immobilized AuNPs exposed to methanol (n = 1.33), 1-propanol (n = 1.38), then back to methanol. ELW = 48 ± 2 nm for all three peaks. (B) The redshift of LSPR peak position as a result of thiolation versus the LSPR peak wavelength before the formation of thiol SAM. Each data point represents a different ensemble/sample. The trend is highlighted with an arrow.

The four premises of the ensemble hypothesis are: (1) AuNPs are immobilized on a substrate; (2) there is a size distribution within an ensemble of AuNPs so that the resonance peak position (λ_0) is controlled by the predominant size and that the half maximum position (λ_1) is determined by larger particles; (3) all AuNPs have similar bulk sensitivity; (4) the ad-layer does not extend far beyond the evanescent decay length of AuNPs.

The first premise is based on the fact that SAM molecules displace the surface anions of chemically reduced colloids, disrupting the repulsive forces that stabilize the suspension.

Thus, the observed optical changes for colloidal plasmonic nanoparticles should largely be attributed to the aggregation of colloids and not to the presence of thiol capping layers.[119-121] The ensemble hypothesis is therefore only valid for surface immobilized nanoparticles. In fact, ensemble peak broadening instead of narrowing has been observed for colloidal plasmonic nanoparticles.[28, 122-123]

The second premise should be valid for a realistic ensemble with a reasonable size distribution as long as the LSPR peak position redshifts as the particle size increases (see Fig. 12).[24, 55, 115] The ensemble spectrum can therefore be described as the sum of single particle spectra multiplied by their respective weighting factors according to the size distribution.[124]

The third premise is supported theoretically[125] as all the AuNPs studied fall within the regime of electrostatic approximation (see section 4.2.3 and Fig. 12 for size measurements). It is also corroborated by the bulk sensing experiment (Fig. 14A) in that all the AuNPs exhibited the same amount of redshift and blueshift reversibly, leading to a constant ELW throughout a cycle of change in bulk refractive index. Moreover, it has been shown explicitly that the bulk sensitivity of surface immobilized AuNPs fall within a narrow range regardless of the size for particles up to 48 nm in diameter.[24] The fourth premise should generally hold true for small organic molecules. Otherwise, the exponentially decaying field will lead to a weak response. Since the decay length is comparable to the particle size, an ad-layer of around 10 nm in thickness is reasonable for simple systems such as biotin-streptavidin, whose swollen thickness is around 6 nm.[126]

4.3.2 Ensemble Hypothesis

For an ensemble of AuNPs, let the diameter and the evanescent decay length of the predominant particle size (peaking at λ_0) denoted by D_0 and I_0; and those of the particles peaking at λ_1 by D_1 and I_1. Quantitatively, the shift of the λ_0 position of an ensemble spectrum ($\Delta\lambda_{LSPR0}$, equation 27) due to a single adsorbed layer of uniform thickness can be expressed in terms of its refractive index (n_a) and thickness (Δd); refractive index of the solvent (n_s); characteristic decay length (I_0) and bulk sensitivity (m) of the nanoparticles.[127] The shift of the λ_1 position ($\Delta\lambda_{LSPR1}$) can be obtained the same way by substituting I_1 for I_0 and λ_1 for λ_0. Therefore, the change in ensemble linewidth (ΔELW, equation 28) can be expressed as the difference between $\Delta\lambda_{LSPR1}$ and $\Delta\lambda_{LSPR0}$ as illustrated in Fig. 13.

$$\lambda_0' - \lambda_0 = \Delta\lambda_{LSPR0} = m(n_a - n_s)(1 - e^{-\frac{2\Delta d}{I_0}}) \tag{27}$$

$$\Delta ELW = \Delta\lambda_{LSPR1} - \Delta\lambda_{LSPR0} = m(n_a - n_s)(e^{-\frac{2\Delta d}{I_0}} - e^{-\frac{2\Delta d}{I_1}}) \tag{28}$$

Given that m, (n_a – n_s), and Δd terms are the same for all sizes within an ensemble, $\Delta\lambda_{LSPR0}$ and ΔELW are entirely determined by the exponential terms in both equations. Since smaller nanoparticles have shorter decay lengths[128], their $1 - e^{-\frac{2\Delta d}{I_0}}$ terms are larger, leading to more pronounced shifts. In fact, smaller particles are more sensitive due to a more confined electromagnetic field and a larger analyte to sensing volume ratio.[93, 129-130] This comparison is supported both theoretically[125] and experimentally (Fig. 14B) where smaller AuNPs peaking at shorter LSPR wavelengths exhibited larger redshifts after the formation of thiol SAM. Since the trend of smaller AuNPs exhibiting higher surface sensitivity is valid for particles up to 80 nm in diameter and an ad-layer of 15 nm in thickness[125], the ensemble hypothesis should be applicable in a wide range of situations as long as the four premises are satisfied. This allows the interpretation of ensemble narrowing observed in the literature [27, 37, 111-114] and ensures the adaptability of the sensing platform we will propose in section 4.3.3.

Within an ensemble of AuNPs, since D_0 is smaller than D_1, $\Delta\lambda_{LSPR0}$ is larger than $\Delta\lambda_{LSPR1}$, the ELW decreases as a result of thiolation. Indeed, the decrease in ELWs for 18 arbitrarily chosen ensembles after being functionalized with the thiol mixture (Fig. 15A) confirms the above conclusion and the narrowing effect observed in the literature.[27, 37, 111-114] In short, the ELW is decreased due to a differential behaviour that arises from the ensemble size distribution: smaller particles corresponding to the blue side of a spectrum display larger redshifts than the larger ones that contribute to the red side of the spectrum.

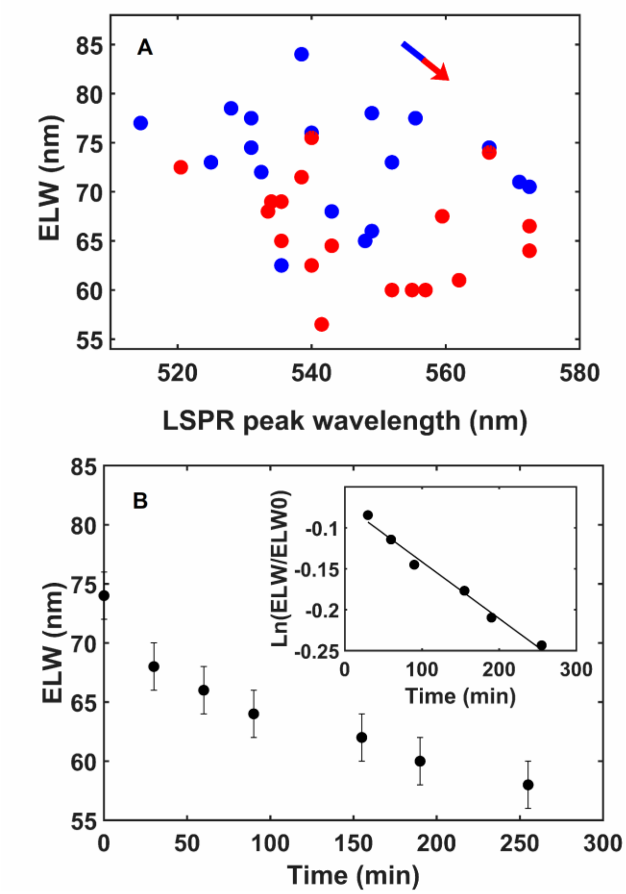

Figure 15. (A) ELWs of different AuNP ensembles before (blue) and after (red) being functionalized with the mixed thiol SAM. The trend is highlighted with an arrow. Each blue point or each red point represents a different ensemble/sample. See Table S4 for their numerical values. The error bars are within the size of the symbols. (B) Time evolution of the ELW for one ensemble of AuNPs during the formation of the mixed thiol SAM. The inset shows a first order kinetic for the ELW with respect to time. All spectra were taken in water.

The time progression of ELW during SAM formation reveals a first order kinetic plot (Fig. 15B) even though the plasmon peak position (λ_0) remains unchanged (see Fig. S1 for raw spectra). Thus, ELW unveils information that might otherwise be lost by monitoring the resonance peak position alone.

4.3.3 ELW for Biosensing

The continuation of ensemble narrowing from SAM formation to analyte binding is observed for AuNPs immobilized on both glass and polystyrene substrates (Fig. 16A and 16B respectively, green triangles). The shift of LSPR peak wavelength (Fig. 16A and 16B, orange circles), on the other hand, increases with a growing thickness and refractive index of the biotin-streptavidin layer.

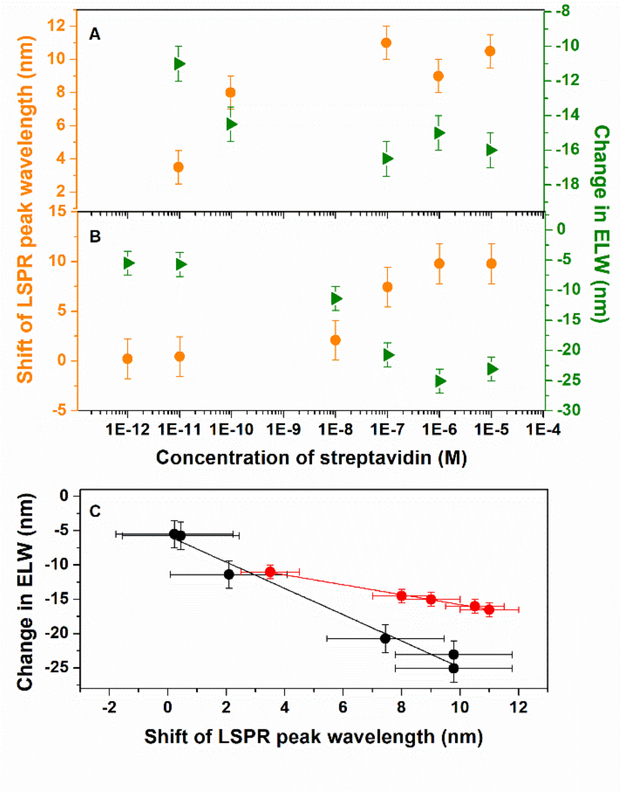

Figure 16. LSPR peak shift (orange circles) and change in ELW (green triangles) with respect to bare AuNPs versus concentration of streptavidin for (A) a glass substrate in water and (B) a polystyrene substrate in air. (C) Linear correlation between the change in ELW and the shift of LSPR peak wavelength. The slope and R^2 are -0.72 and 0.99 for the glass substrate (red); -1.9 and 0.98 for the polystyrene substrate (black).

Because there will always be some degree of surface defects in SAM layers over the probing area of the UV-vis spectrometer, as can be confirmed by the broad distribution of shift response in Fig. 14B, the bound streptavidin and the biotinylated SAM are regarded as one single ad-layer. In fact, treating two imperfect layers as separate entities distorts the estimation of n_a.[126] Therefore equation 27 and 28 are still valid, with $\Delta\lambda_{LSPR0}$ and ΔELW describing the shift of LSPR peak wavelength and the change in ensemble linewidth with respect to bare AuNPs in an aqueous environment.

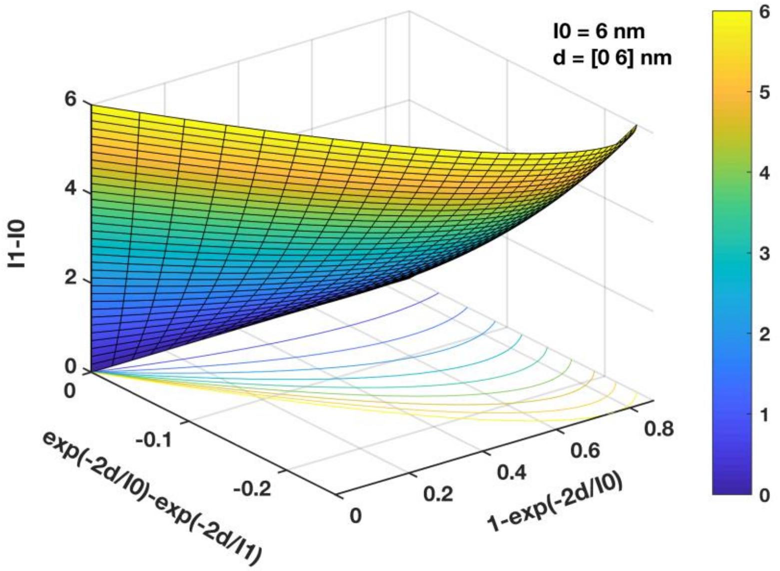

Figure 17. The change in ELW (ΔELW) and the shift of LSPR wavelength ($\Delta LSPR_0$) are proportional to $\boldsymbol{(e^{-\frac{2\Delta d}{I_0}} - e^{-\frac{2\Delta d}{I_1}})}$ and $\boldsymbol{(1 - e^{-\frac{2\Delta d}{I_0}})}$ respectively. ΔELW and $\Delta LSPR_0$ exhibit a quasi-linear relationship when the ad-layer thickness (d) is within about 5 nm, given that the decay length I_0 is assumed to be 6 nm. This linear correlation is valid for different values of (I_1-I_0), and the slope is steeper with a broader size distribution. [0,6] nm is chosen to be the range of d because 6 nm is the reported thickness for a swollen biotin-streptavidin layer.[131]

As more streptavidin molecules bind to biotin, Δd and (n_a – n_s) increase as functions of streptavidin concentration. Again, the m, Δd and (n_a – n_s) terms are the same for all the nanoparticles within a population. Plotting $e^{-\frac{2\Delta d}{I_0}} - e^{-\frac{2\Delta d}{I_1}}$ versus $1 - e^{-\frac{2\Delta d}{I_0}}$ gives a quasi-linear correlation between ΔELW and $\Delta LSPR_0$, as long as Δd is still comparable to I_0 (Fig. 17). The predicted linearity is corroborated for AuNPs on both glass and polystyrene substrates (Fig. 16C). Furthermore, the theoretical slope of this quasi-linear relationship becomes steeper with an increasing difference between I_0 and I_1 (Fig. 17). Since a broad size distribution (large I_1-I_0) entails a large resonance linewidth that decreases the figure of merit (FOM) of plasmonic nanoparticles,[1] monitoring the change in ELW instead of wavelength shift proves more advantageous when the slope is steeper than negative one; where the slope is determined by the values of Δd, I_0 and I_1. The linearity between ELW and LSPR peak position urges for a new sensing avenue.

Rather than a stand-alone sensing pathway, registering both ELW and LSPR peak wavelength imparts comprehensiveness, flexibility and portability. This can be achieved with a simplified transmission-based platform consisting of a prism and a photodiode array (Fig. 18) that disperses and detects the transmitted white light sequentially. Without any moving component, this configuration can be miniaturized more readily. ELW encodes more spectral information than LSPR wavelength alone; but the latter requires less computational effort and memory space, because ELW is calculated based on the pixel distance between λ_0 and λ_1 rather than the pixel position of λ_0 alone. Users should be able to choose either or both of the parameters depending on their needs.

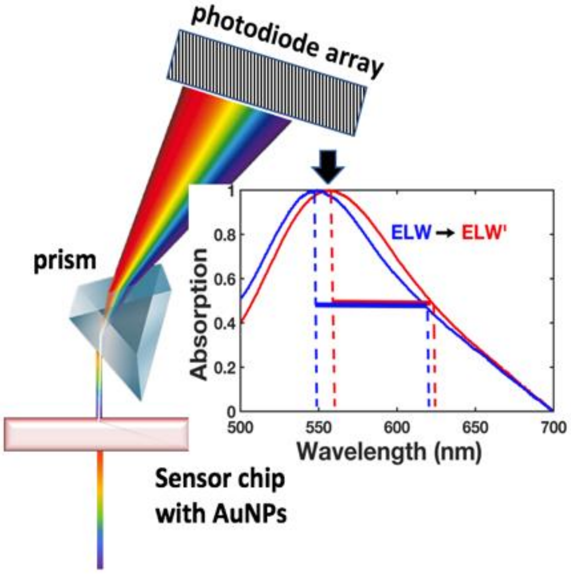

Figure 18. The proposed portable sensing platform that can monitor the change in both LSPR peak wavelength and ELW.

Since ELW is calculated as the pixel distance between λ_0 and λ_1, the measurement uncertainty is double of what would be for reading the peak shift alone. However, S/N can be enhanced by smoothing algorithm such as peak centroid fitting if necessary.[132] Curvature has been proved useful for monitoring spectral changes without the influence of zeroth and first order noise such as drift and tilt.[27] However, taking second derivative of absorption with respect to wavelength needs to be performed graphically, thus is not suitable for a portable device with real-time readout. These types of noise can be minimized by integrated a series of algorithms: Fourier transform, digital filters, and then an inverse Fourier transform. The methods stated here are all extrinsic methods that can be applied in conjunction with other intrinsic improvements outlined in the Introduction to further enhance the sensitivity and S/N.

4.4 Conclusion

The narrowing of ELW observed in the literature [27, 37, 111-114] can be explained by a differential shifting behaviour that arises from the ensemble size distribution as the thickness of adsorbed layers increases. This ensemble hypothesis is corroborated by the experimental evidence presented herein. While both are a function of analyte concentration, ELW reveals more spectral details than plasmon peak position, and can lead to a higher FOM if the slope of Δ ELW versus $\Delta LSPR_0$ is steeper than negative one. A portable transmission-based sensing platform allowing the simultaneous measurement of both LSPR wavelength and ELW is proposed. In comparison to conventional sensing configurations, the proposed platform not only reveals more spectral details and permits real-time measurements, but also present a possibility of sensitivity enhancement and miniaturization. This platform can also be adapted for other types of plasmonic nanoaprticles with different size ranges and geometries as long as the four premises of the ensemble hypothesis are satisfied.

4.5 References

91. Link, S.; El-Sayed, M. A., Size and Temperature Dependence of the Plasmon Absorption of Colloidal Gold Nanoparticles. *The Journal of Physical Chemistry B* **1999,** *103* (21), 4212-4217.

92. Link, S.; El-Sayed, M. A., Shape and size dependence of radiative, non-radiative and photothermal properties of gold nanocrystals. *International Reviews in Physical Chemistry* **2000,** *19* (3), 409-453.

93. Anker, J. N.; Hall, W. P.; Lyandres, O.; Shah, N. C.; Zhao, J.; Van Duyne, R. P., Biosensing with plasmonic nanosensors. *Nature Materials* **2008,** *7* (6), 442-453.

94. Willets, K. A.; Duyne, R. P. V., Localized Surface Plasmon Resonance Spectroscopy and Sensing. *Annual Review of Physical Chemistry* **2007,** *58* (1), 267-297.

95. Johansen, K.; Stålberg, R.; Lundström, I.; Liedberg, B., Surface plasmon resonance: instrumental resolution using photo diode arrays. *Measurement Science and Technology* **2000,** *11* (11), 1630.

96. Johansen, K.; Lundström, I.; Liedberg, B., Sensitivity deviation: instrumental linearity errors that influence concentration analyses and kinetic evaluation of biomolecular interactions. *Biosensors and Bioelectronics* **2000,** *15* (9), 503-509.

97. Shiohara, A.; Novikov, S. M.; Solís, D. M.; Taboada, J. M.; Obelleiro, F.; Liz-Marzán, L. M., Plasmon Modes and Hot Spots in Gold Nanostar–Satellite Clusters. *The Journal of Physical Chemistry C* **2015,** *119* (20), 10836-10843.

98. Lee, T. K.; Kwak, S. K., Effects of LSPR of Gold Nanospheres by Surface Vacancies and Protruding Tips. *The Journal of Physical Chemistry C* **2014,** *118* (11), 5881-5888.

99. Shen, Y.; Zhou, J.; Liu, T.; Tao, Y.; Jiang, R.; Liu, M.; Xiao, G.; Zhu, J.; Zhou, Z.-K.; Wang, X.; Jin, C.; Wang, J., Plasmonic gold mushroom arrays with refractive index sensing figures of merit approaching the theoretical limit. *Nature Communications* **2013,** *4*, 2381.

100. King, N. S.; Liu, L.; Yang, X.; Cerjan, B.; Everitt, H. O.; Nordlander, P.; Halas, N. J., Fano Resonant Aluminum Nanoclusters for Plasmonic Colorimetric Sensing. *ACS Nano* **2015,** *9* (11), 10628-10636.

101. Nugroho, F. A. A.; Iandolo, B.; Wagner, J. B.; Langhammer, C., Bottom-Up Nanofabrication of Supported Noble Metal Alloy Nanoparticle Arrays for Plasmonics. *ACS Nano* **2016,** *10* (2), 2871-2879.

102. Ferhan, A. R.; Kim, D.-H., Nanoparticle polymer composites on solid substrates for plasmonic sensing applications. *Nano Today* **2016,** *11* (4), 415-434.

103. Skoog, D. A.; Holler, F. J.; Crouch, S. R., *Principles of Instrumental Analysis*. Cengage Learning: 2017.

104. Piscevic, D.; Knoll, W.; Tarlov, M. J., Surface plasmon microscopy of biotin-streptavidin binding reactions on UV-photopatterned alkanethiol self-assembled monolayers. *Supramolecular Science* **1995,** *2* (2), 99-106.

105. Spinke, J.; Liley, M.; Schmitt, F. J.; Guder, H. J.; Angermaier, L.; Knoll, W., Molecular recognition at self-assembled monolayers: Optimization of surface functionalization. *The Journal of Chemical Physics* **1993,** *99* (9), 7012-7019.

106. Zijlstra, P.; Paulo, P. M. R.; Yu, K.; Xu, Q.-H.; Orrit, M., Chemical Interface Damping in Single Gold Nanorods and Its Near Elimination by Tip-Specific Functionalization. *Angewandte Chemie International Edition* **2012,** *51* (33), 8352-8355.

107. Foerster, B.; Joplin, A.; Kaefer, K.; Celiksoy, S.; Link, S.; Sönnichsen, C., Chemical Interface Damping Depends on Electrons Reaching the Surface. *ACS Nano* **2017,** *11* (3), 2886-2893.

108. Kreibig, U., Interface-induced dephasing of Mie plasmon polaritons. *Applied Physics B* **2008,** *93* (1), 79-89.

109. Douglas-Gallardo, O. A.; Berdakin, M.; Sánchez, C. G., Atomistic Insights into Chemical Interface Damping of Surface Plasmon Excitations in Silver Nanoclusters. *The Journal of Physical Chemistry C* **2016,** *120* (42), 24389-24399.

110. Hövel, H.; Fritz, S.; Hilger, A.; Kreibig, U.; Vollmer, M., Width of cluster plasmon resonances: Bulk dielectric functions and chemical interface damping. *Physical Review B* **1993,** *48* (24), 18178-18188.

111. Hall, W. P.; Ngatia, S. N.; Van Duyne, R. P., LSPR Biosensor Signal Enhancement Using Nanoparticle−Antibody Conjugates. *The Journal of Physical Chemistry C* **2011,** *115* (5), 1410-1414.

112. Oh, S. Y.; Heo, N. S.; Shukla, S.; Cho, H.-J.; Vilian, A. T. E.; Kim, J.; Lee, S. Y.; Han, Y.-K.; Yoo, S. M.; Huh, Y. S., Development of gold nanoparticle-aptamer-based LSPR sensing chips for the rapid detection of Salmonella typhimurium in pork meat. *Scientific Reports* **2017,** *7* (1), 10130.

113. Barbillon, G., Plasmonic Nanostructures Prepared by Soft UV Nanoimprint Lithography and Their Application in Biological Sensing. *Micromachines* **2012,** *3* (1).

114. Endo, T.; Kerman, K.; Nagatani, N.; Takamura, Y.; Tamiya, E., Label-Free Detection of Peptide Nucleic Acid−DNA Hybridization Using Localized Surface Plasmon Resonance Based Optical Biosensor. *Analytical Chemistry* **2005,** *77* (21), 6976-6984.

115. Ertorer, E. Fabricating Cost-Effective Nanostructures for Biomedical Applications. The University of Western ontario, London, ON, 2013.

116. Guerrisi, M.; Rosei, R.; Winsemius, P., Splitting of the interband absorption edge in Au. *Physical Review B* **1975,** *12* (2), 557-563.

117. Ngoc, L. L. T.; Wiedemair, J.; van den Berg, A.; Carlen, E. T., Plasmon-modulated photoluminescence from gold nanostructures and its dependence on plasmon resonance, excitation energy, and band structure. *Optics Express* **2015,** *23* (5), 5547-5564.

118. Aspnes, D. E.; Kinsbron, E.; Bacon, D. D., Optical properties of Au: Sample effects. *Physical Review B* **1980,** *21* (8), 3290-3299.

119. Mirkin, C. A.; Letsinger, R. L.; Mucic, R. C.; Storhoff, J. J., A DNA-based method for rationally assembling nanoparticles into macroscopic materials. *Nature* **1996,** *382* (6592), 607-609.

120. Malinsky, M. D.; Kelly, K. L.; Schatz, G. C.; Van Duyne, R. P., Chain Length Dependence and Sensing Capabilities of the Localized Surface Plasmon Resonance of

Silver Nanoparticles Chemically Modified with Alkanethiol Self-Assembled Monolayers. *Journal of the American Chemical Society* **2001,** *123* (7), 1471-1482.

121. Weisbecker, C. S.; Merritt, M. V.; Whitesides, G. M., Molecular Self-Assembly of Aliphatic Thiols on Gold Colloids. *Langmuir* **1996,** *12* (16), 3763-3772.

122. Linnert, T.; Mulvaney, P.; Henglein, A., Surface chemistry of colloidal silver: surface plasmon damping by chemisorbed iodide, hydrosulfide (SH-), and phenylthiolate. *The Journal of Physical Chemistry* **1993,** *97* (3), 679-682.

123. Crespo, P.; Litrán, R.; Rojas, T. C.; Multigner, M.; de la Fuente, J. M.; Sánchez-López, J. C.; García, M. A.; Hernando, A.; Penadés, S.; Fernández, A., Permanent Magnetism, Magnetic Anisotropy, and Hysteresis of Thiol-Capped Gold Nanoparticles. *Physical Review Letters* **2004,** *93* (8), 087204.

124. Hu, Z. J.; Hou, S.; Ji, Y. L.; Wen, T.; Liu, W. Q.; Zhang, H.; Shi, X. W.; Yan, J.; Wu, X. C., Fast characterization of gold nanorods ensemble by correlating its structure with optical extinction spectral features. *AIP Advances* **2014,** *4* (11), 117137.

125. Kvasnička, P.; Homola, J., Optical sensors based on spectroscopy of localized surface plasmons on metallic nanoparticles: Sensitivity considerations. *Biointerphases* **2008,** *3* (3), FD4-FD11.

126. Mittler, S.; Menges, B., Evanescent Waves as Nanoprobes for Surfaces and Interfaces: From Waveguide Technology to Sensor Application. In *Frontiers in Surface Nanophotonics: Principles and Applications*, Andrews, D. L.; Gaburro, Z., Eds. Springer New York: New York, NY, 2007; pp 19-47.

127. Jung, L. S.; Campbell, C. T.; Chinowsky, T. M.; Mar, M. N.; Yee, S. S., Quantitative Interpretation of the Response of Surface Plasmon Resonance Sensors to Adsorbed Films. *Langmuir* **1998,** *14* (19), 5636-5648.

128. Huang, X.; El-Sayed, M. A., Gold nanoparticles: Optical properties and implementations in cancer diagnosis and photothermal therapy. *Journal of Advanced Research* **2010,** *1* (1), 13-28.

129. Kedem, O.; Tesler, A. B.; Vaskevich, A.; Rubinstein, I., Sensitivity and Optimization of Localized Surface Plasmon Resonance Transducers. *ACS Nano* **2011,** *5* (2), 748-760.

130. Beeram, S. R.; Zamborini, F. P., Effect of Protein Binding Coverage, Location, and Distance on the Localized Surface Plasmon Resonance Response of Purified Au Nanoplates Grown Directly on Surfaces. *The Journal of Physical Chemistry C* **2011,** *115* (15), 7364-7371.

131. Busse, S.; Scheumann, V.; Menges, B.; Mittler, S., Sensitivity studies for specific binding reactions using the biotin/streptavidin system by evanescent optical methods. *Biosensors and Bioelectronics* **2002,** *17* (8), 704-710.

132. Nusz, G. J.; Marinakos, S. M.; Curry, A. C.; Dahlin, A.; Höök, F.; Wax, A.; Chilkoti, A., Label-Free Plasmonic Detection of Biomolecular Binding by a Single Gold Nanorod. *Analytical Chemistry* **2008,** *80* (4), 984-989.

5 Conclusion and Future Work

In this work, it has been shown that the compact design of a waveguide-plasmonic hybrid sensor not only allows quantitative evaluation of analytes, but also proves more sensitive than the conventional transmission-based plasmonic sensors. In comparison to conventional LSPR sensors, this system is less susceptible to optical noise and positional variation of signals. Moreover, it enables more freedom in the exploitation of plasmonic hot spots with both transverse electric (TE) and transverse magnetic (TM) modes. Through real-time measurement, it is demonstrated that the current sensing system is more sensitive than comparable optical fiber plasmonic sensors. The highest normalized bulk sensitivity (7.744 RIU^{-1}) is found in the TM_1 mode. Biosensing with the biotin-streptavidin system shows that the detection limit is on the order of 10^{-14} M for streptavidin.

Future work includes replacing the glass substrate with a polymer substrate so that the platform is more structurally robust. By directing the incoming beam into multiple optical fibres that are coupled to a multi-channel waveguide, the signal to noise ratio can be significantly improved and the platform can be transformed into a multiplexed system.

It has also been shown that ELW exhibits a linear correlation with respect to the local refractive index. This behaviour stems from the size distribution of an ensemble of plasmonic nanoparticles and the superior surface sensitivity of smaller nanoparticles when the thickness of the analyte layer is still comparable to the particle size. Future work includes the construction of the proposed sensing platform and the testing of its sensitivities using both bulk sensing and bio-sensing experiments.

The two platforms discussed in this thesis have great potentials for practical applications. With further optimization, the sensing systems can easily be mass-produced and incorporated into high throughput screening devices, detecting a variety of chemical and biological analytes via immobilization of the appropriate recognition sites.

Appendix

Appendix A: Copyright Permissions

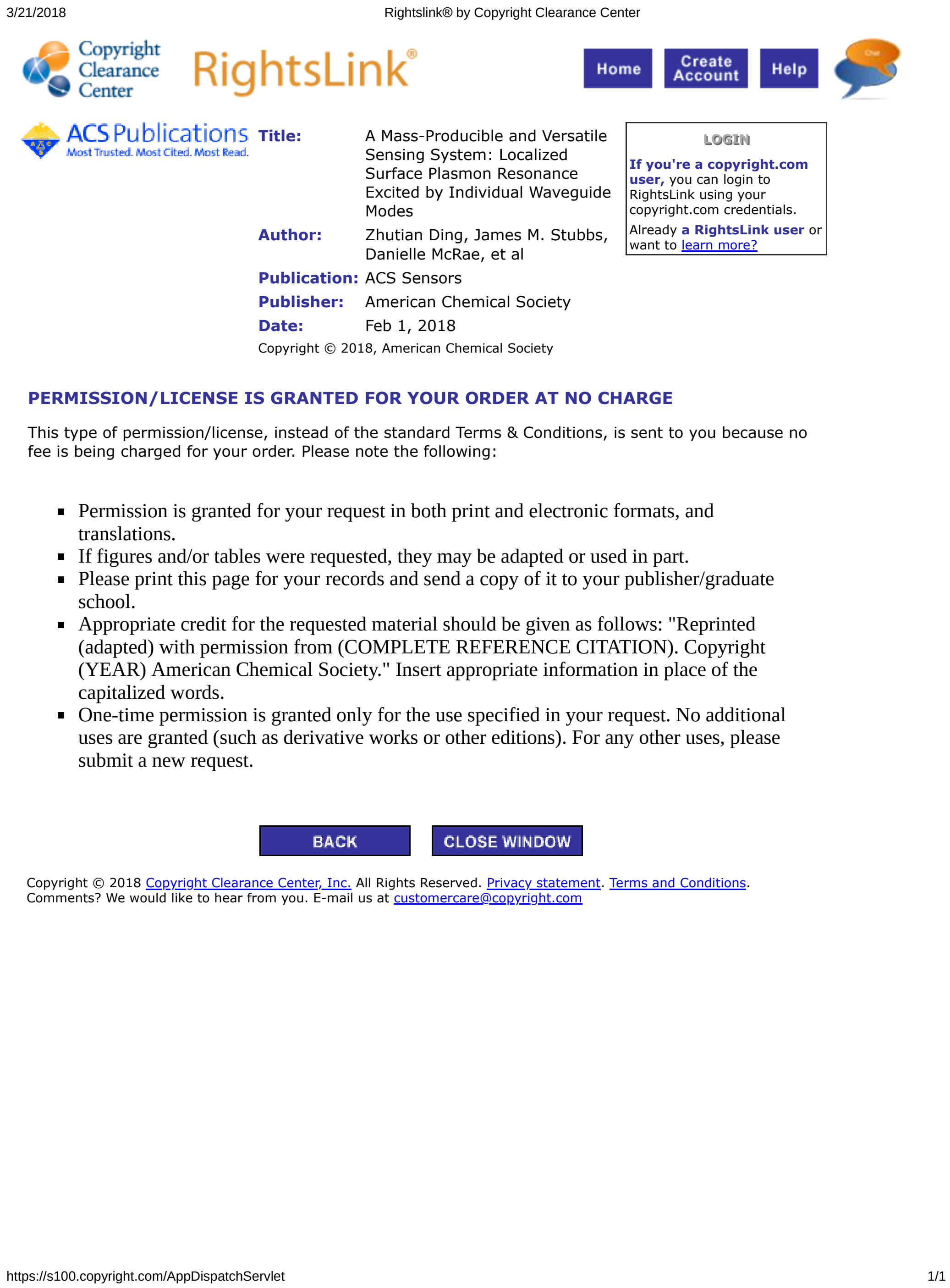

3/21/2018 Rightslink® by Copyright Clearance Center

Title:	A Mass-Producible and Versatile Sensing System: Localized Surface Plasmon Resonance Excited by Individual Waveguide Modes
Author:	Zhutian Ding, James M. Stubbs, Danielle McRae, et al
Publication:	ACS Sensors
Publisher:	American Chemical Society
Date:	Feb 1, 2018

Copyright © 2018, American Chemical Society

LOGIN

If you're a copyright.com user, you can login to RightsLink using your copyright.com credentials.
Already **a RightsLink user** or want to learn more?

PERMISSION/LICENSE IS GRANTED FOR YOUR ORDER AT NO CHARGE

This type of permission/license, instead of the standard Terms & Conditions, is sent to you because no fee is being charged for your order. Please note the following:

- Permission is granted for your request in both print and electronic formats, and translations.
- If figures and/or tables were requested, they may be adapted or used in part.
- Please print this page for your records and send a copy of it to your publisher/graduate school.
- Appropriate credit for the requested material should be given as follows: "Reprinted (adapted) with permission from (COMPLETE REFERENCE CITATION). Copyright (YEAR) American Chemical Society." Insert appropriate information in place of the capitalized words.
- One-time permission is granted only for the use specified in your request. No additional uses are granted (such as derivative works or other editions). For any other uses, please submit a new request.

Copyright © 2018 Copyright Clearance Center, Inc. All Rights Reserved. Privacy statement. Terms and Conditions.
Comments? We would like to hear from you. E-mail us at customercare@copyright.com

https://s100.copyright.com/AppDispatchServlet 1/1

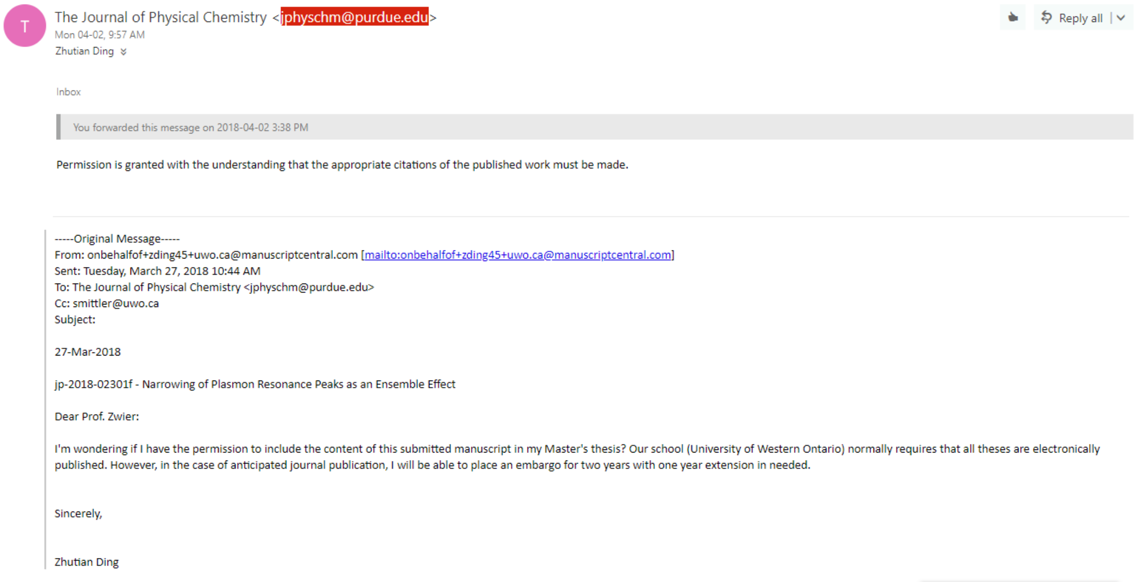

The Journal of Physical Chemistry <jphyschm@purdue.edu>
Mon 04-02, 9:57 AM
Zhutian Ding

You forwarded this message on 2018-04-02 3:38 PM

Permission is granted with the understanding that the appropriate citations of the published work must be made.

-----Original Message-----
From: onbehalfof+zding45+uwo.ca@manuscriptcentral.com [mailto:onbehalfof+zding45+uwo.ca@manuscriptcentral.com]
Sent: Tuesday, March 27, 2018 10:44 AM
To: The Journal of Physical Chemistry <jphyschm@purdue.edu>
Cc: smittler@uwo.ca
Subject:

27-Mar-2018

jp-2018-02301f - Narrowing of Plasmon Resonance Peaks as an Ensemble Effect

Dear Prof. Zwier:

I'm wondering if I have the permission to include the content of this submitted manuscript in my Master's thesis? Our school (University of Western Ontario) normally requires that all theses are electronically published. However, in the case of anticipated journal publication, I will be able to place an embargo for two years with one year extension in needed.

Sincerely,

Zhutian Ding

Appendix B: Supporting Information for Chapter 3.

Table S1. Parameters for m-line peaks.

		TM_0	TM_1	TE_0	TE_1
Bare waveguide	Coupling angle (± 0.025°)	33.775	30.250	33.625	30.400
	Peak intensity I_{max} (± 0.1 mV)	1.6	7.5	4.8	25.1
	FWHM (°)	0.085	0.099	0.084	0.097
	IOWA (°/mV)	0.0531 ± 0.0033	0.0132 ± 0.0002	0.0175 ± 0.0004	0.00386 ± 0.00002
After gold deposition	Coupling angle (± 0.025°)	33.825	30.200	33.675	30.400
	Peak intensity I_{max} (± 0.1 mV)	1.2	3.0	1.2	3.3
	FWHM (°)	0.086	0.081	0.088	0.087
	IOWA (°/mV)	0.0717 ± 0.0060	0.0270 ± 0.0009	0.0733 ± 0.0061	0.0264 ± 0.0008
	IONA	0.36 ± 0.05	1.0 ± 0.1	3.0 ± 0.3	5.8 ± 0.2

Table S2. Average waveguide transmission* for each liquid medium.

Average waveguide transmission	TM_0 (± 0.002 mV)	TM_1 (± 0.003 mV)	TE_0 (± 0.002 mV)	TE_1 (± 0.005 mV)
Water	1.675	3.986	1.557	3.696
2%	1.689	4.010	1.567	3.711
4%	1.701	4.064	1.570	3.728
5%	1.711	NA	1.574	3.737
7%	1.723	4.145	1.580	3.769
9%	1.731	4.263	1.585	3.781
11%	1.740	4.328	1.591	3.821
13% glycerol	1.748	4.408	1.597	3.852

*Outliers were excluded for average calculation.

Appendix C: Supporting Information for Chapter 4.

Table S3. Estimated ELW values from the literature before and after SAM formation and analyte binding.[27, 37, 111-114]

Fig. in ref.	Fabrication method; type of plasmonic nanoparticles	SAM	Recognition reaction	*ELW (nm)		
				Bare	After SAM formation	After analyte binding
Fig. 2B[111]	Nanosphere lithography; silver	Octanethiol/11-mercaptoundecanoic acid + amine conjugated biotin	Biotin-antibiotin	N.A.	97.5 ± 2.5	92.5 ± 2.5
Fig. 4[113]	UV nanoprint lithography; gold	Trithiolated polypeptites modified with biotin at their N-terminals	Biotin-streptavidin	51.8 ± 0.9	50.9 ± 0.9	40.1 ± 0.9
Fig. 2D[112]	Citrate reduced colloids immobilized with silanes; gold	Thrombin binding aptamers	Aptamer - *S. typhimurium*	50.0 ± 1.2	50.0 ± 1.2	47.6 ± 1.2
Fig. 4B[37]	Physical vapor deposition onto silica nanoparticles; gold	Probe DNA with a single mutation	DNA-DNA	46.7 ± 1.1	42.2 ± 1.1	41.1 ± 1.1 (1 μM target DNA)
Fig. 5A[114]	Thermal deposition onto silica nanoparticles;	Peptide nucleic acid (PNA)	PNA-DNA	31.9 ± 1.4	30.6 ± 1.4	26.4 ± 1.4 (1 μM target DNA)

	gold					
Fig. 5A[27]	Citrate reduced colloids immobilized with silanes; gold	SH-PEG$_7$-COOH	N/A	70.6 ± 2.9	52.9 ± 2.9	N/A

*The estimated ELW values were obtained by measuring the physical distance between λ_0 and λ1, and then convert the physical distance to spectral distance by using the corresponding wavelength axis as a scale bar. Please see Fig. 13 and the Experimental section for the definition of λ_0 and λ1.

Table S4. Numerical values for data points in Fig. 2A. LSPR wavelength and ELW for 18 arbitrarily chosen samples before and after functionalization with biotinylated thiol.

	LSPR peak wavelength ± 0.25 (nm)		ELW ± 0.5 (nm)	
Name (arbitrary)	bare	thiol	bare	thiol
9B	571.0	572.5	71.0	64.0
13D	528.0	533.5	78.5	68.0
14B	532.5	535.5	72.0	65.0
14D	514.5	520.5	77.0	72.5
15C	538.5	540.0	84.0	62.5
15D	525.0	534.0	73.0	69.0

16C	543.0	543.0	68.0	64.5
17B	555.5	559.5	77.5	67.5
17C	548.0	552.0	65.0	60.0
17D	549.0	557.0	66.0	60.0
17E	549.0	555.0	78.0	60.0
18B	552.0	562.0	73.0	61.0
18C	572.5	572.5	70.5	66.5
18D	566.5	566.5	74.5	74.0
18E	535.5	541.5	62.5	56.5
19A	531.0	535.5	74.5	69.0
19D	540.0	540.0	76.0	75.5
20A	531.0	538.5	77.5	71.5

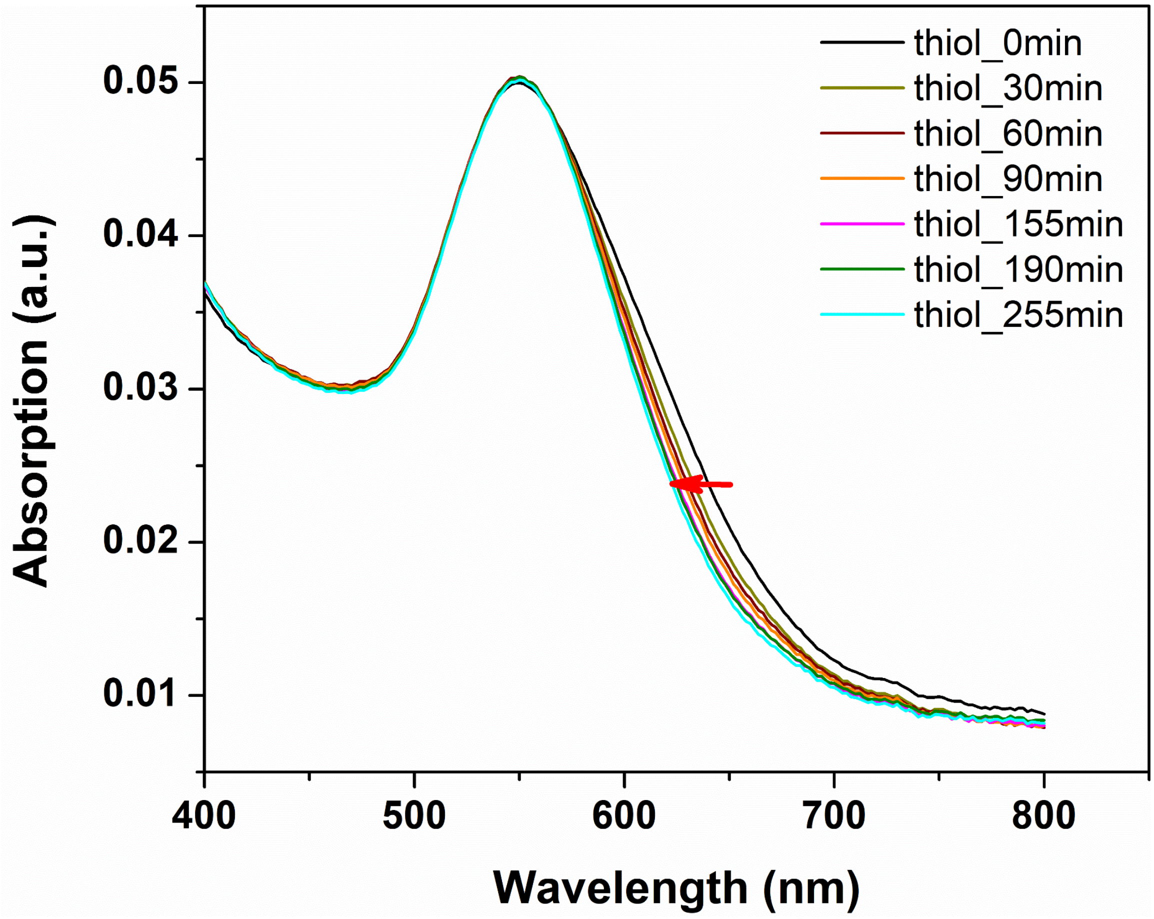

Figure S1. During the formation of the mixed thiol SAM, the ELW decreases whereas the plasmon peak position stays unchanged. All spectra are unprocessed. An arbitrary sample was measured here.

Curriculum Vitae

Name:	Zhutian Ding
Post-secondary Education and Degrees:	McGill University Montréal, Québec, Canada 2010-2014 BSc
Related Work Experience	Teaching Assistant The University of Western Ontario London, Ontario, Canada 2016-2018

Publications:

Ding Z., Stubbs J., Mittler S., Narrowing of Plasmon Resonance Peaks as an Ensemble Effect. In press. *The Journal of Physical Chemistry C* **2018**.

Ding Z., Stubbs J., McRae D., Blacquiere J., Lagugné-Labarthet F., Mittler S., A Mass-Producible and Versatile Sensing System: Localized Surface Plasmon Resonance Excited by Individual Waveguide Modes. *ACS Sensors* **2018**, 3(2): 334-341.

Lincoln R.; Greene L. E.; Krumova K.; **Ding Z.**; Cosa G., Electronic Excited State Redox Properties for BODIPY Dyes Predicted from Hammett Constants: Estimating the Driving Force of Photoinduced Electron Transfer. *J. Phys. Chem. A* **2014**, 118 (45), 10622-10630.

Conference Participation:

Ding Z., Stubbs J., Blacquiere J and Mittler S. Gold Nanoparticles Bound to Polymer Channel Waveguides for Sensing Applications. Poster presented at Chemical Biophysics Symposium 2017 in Toronto.

Nano Ontario Conference 2016 in Guelph, Ontario.

Ding Z., Lincoln R, Cosa G. Tuning the Fluorogenic Properties of BODIPY Dyes by the Manipulation of Redox Properties Based on Linear Free Energy Relationships. Poster presented at McGill Undergraduate Research Conference 2013 in Montreal.

Graduate Courses Taken at UWO:

CHEM 9674 Spectroscopy and Microscopy, CHEM 9572 Spectro-electr-chemistry, PHYS 9404 Statistical Physics (audit).